

# UCSF

## UC San Francisco Previously Published Works

### Title

The genomic landscapes of individual melanocytes from human skin

### Permalink

<https://escholarship.org/uc/item/47b6v2fv>

### Journal

Nature, 586(7830)

### ISSN

0028-0836

### Authors

Tang, Jessica  
Fewings, Eleanor  
Chang, Darwin  
[et al.](#)

### Publication Date

2020-10-22

### DOI

10.1038/s41586-020-2785-8

Peer reviewed



Published in final edited form as:

*Nature*. 2020 October ; 586(7830): 600–605. doi:10.1038/s41586-020-2785-8.

## The genomic landscapes of individual melanocytes from human skin

Jessica Tang<sup>1,2,\*</sup>, Eleanor Fewings<sup>1,2,\*</sup>, Darwin Chang<sup>1,2</sup>, Hanlin Zeng<sup>3</sup>, Shanshan Liu<sup>1,2</sup>, Aparna Jorapur<sup>1,2</sup>, Rachel L. Belote<sup>3,4</sup>, Andrew S. McNeal<sup>1,2</sup>, Tuyet M. Tan<sup>1,2</sup>, Iwei Yeh<sup>1,2</sup>, Sarah T. Arron<sup>1,2</sup>, Robert L. Judson-Torres<sup>3,4,&</sup>, Boris C. Bastian<sup>1,2,&</sup>, A. Hunter Shain<sup>1,2</sup>

<sup>1</sup>University of California San Francisco, Department of Dermatology

<sup>2</sup>University of California San Francisco, Helen Diller Family Comprehensive Cancer Center

<sup>3</sup>University of Utah, Department of Dermatology

<sup>4</sup>University of Utah, Huntsman Cancer Institute

### Abstract

Every cell in the human body has a unique set of somatic mutations, yet it remains difficult to comprehensively genotype an individual cell<sup>1</sup>. Here, we developed solutions to overcome this obstacle in the context of normal human skin, thus offering the first glimpse into the genomic landscapes of individual melanocytes from human skin. As expected, sun-shielded melanocytes had fewer mutations than sun-exposed melanocytes. However, within sun-exposed sites, melanocytes on chronically sun-exposed skin (e.g. the face) displayed a lower mutation burden than melanocytes on intermittently sun-exposed skin (e.g. the back). Melanocytes located adjacent to a skin cancer had higher mutation burdens than melanocytes from donors without skin cancer,

---

Users may view, print, copy, and download text and data-mine the content in such documents, for the purposes of academic research, subject always to the full Conditions of use:[http://www.nature.com/authors/editorial\\_policies/license.html#terms](http://www.nature.com/authors/editorial_policies/license.html#terms) Reprints and permissions information is available at [www.nature.com/reprints](http://www.nature.com/reprints)

Address correspondence to Alan.Shain@ucsf.edu (AHS), Correspondence and requests for materials should be addressed to A. Hunter Shain.

\*These authors contributed equally

&These authors jointly supervised this work

Author Contributions

Conception and design of the work: A. Hunter Shain. Data collection: Jessica Tang, Darwin Chang, Shanshan Liu, Eleanor Fewings, Hanlin Zeng, Aparna Jorapur, Rachel L. Belote, Andrew S. McNeal, Sarah T. Arron. Data analysis and interpretation: Eleanor Fewings, Jessica Tang, Darwin Chang, Tuyet M. Tan, Robert L. Judson-Torres, Boris C. Bastian, A. Hunter Shain. Drafting the article: Eleanor Fewings, Jessica Tang, A. Hunter Shain. Critical revision of the article: Eleanor Fewings, Jessica Tang, A. Hunter Shain, Rachel L. Belote, Iweh Yeh, Sarah T. Arron, Robert L. Judson-Torres, Boris C. Bastian.

Data Availability

Sequence data has been deposited in dbGaP with the accession code phs001979.v1.p1.

Code Availability

Scripts and resources to perform analyses downstream of variant calling are available on GitHub ([https://github.com/elliefewings/Melanocytes\\_Tang2020](https://github.com/elliefewings/Melanocytes_Tang2020)).

Competing Interests Declaration

STA is an employee at Rakuten Medical and a consultant for Castle Biosciences and Enspectra Health.

Extended Dataset

Extended dataset is available online-only through *Nature*. Individual sample summaries of every single cell clone is hosted by figshare (<https://figshare.com/s/bb5614d5ab4554516278>).<sup>21</sup>

Supplementary Information

Supplementary tables are available online-only through *Nature*.

implying that the mutation burden of normal skin can be harnessed to measure cumulative sun damage and skin cancer risk. Moreover, melanocytes from healthy skin commonly harbor pathogenic mutations, though these mutations tended to be weakly oncogenic, likely explaining why they did not give rise to discernible lesions. Phylogenetic analyses identified groups of related melanocytes, suggesting that melanocytes spread throughout skin as fields of clonally related cells, invisible to the naked eye. Overall, our study offers an unprecedented view into the genomic landscapes of individual melanocytes, revealing key insights into the causes and origins of melanoma.

---

Cutaneous melanomas are skin cancers that arise from melanocytes, the pigment producing cells in the skin. Thousands of melanomas have been sequenced to date, revealing a high burden of somatic mutations with patterns implicating sunlight as the major mutagen responsible for their formation. It is currently unknown precisely when these mutations are acquired during the course of tumorigenesis and whether their rate of accumulation accelerates during neoplastic transformation.

In normal skin, melanocytes reside within the penetrable range of UV-A and UV-B radiation in the basilar epidermis. They make up a minor fraction of the cells in the epidermis, which is mainly comprised of keratinocytes. Keratinocytes have a p53-dependent program that triggers apoptosis after exposure to high doses of UV radiation, resulting in the sloughing off of epidermal sheets after a sunburn<sup>2</sup>. As a result, clonal patches of *TP53*-mutant keratinocytes are prevalent in sun-exposed skin<sup>3,4</sup>, and these can eventually give rise to keratinocyte cancers.

By contrast, the homeostatic mechanisms governing melanocytes and selective pressures operating on melanocytes during early phases of transformation are less well understood. While some melanomas arise from nevi (i.e. common moles), most arise in the absence of a precursor lesion. Understanding the mutational processes and kinetics of mutation acquisition in pre-malignant melanocytes of normal skin would provide important insights into the early phases of transformation, before clinically visible neoplastic proliferations have formed.

Most DNA sequencing studies are performed on a bulk group of cells, yielding an average signal from the complex mixture of cells that are sampled. Bulk-cell sequencing of normal blood<sup>5</sup>, skin<sup>4</sup>, esophageal mucosa<sup>6</sup>, and colonic crypts<sup>7</sup> has identified mutations in these tissues, including the presence of pathogenic mutations, offering valuable insights into the earliest phases of carcinogenesis in these tissue types. However, bulk-cell sequencing is not suited to detect mutations in melanocytes because melanocytes are sparsely distributed in the skin<sup>4</sup>.

Genotyping studies at the resolution of individual cells are rare and none have been performed on melanocytes. Genotyping an individual cell is difficult because there is only one molecule of dsDNA corresponding to each parental allele in a diploid cell. There are primarily two strategies to overcome this bottleneck. First, an individual cell can be sequenced after amplifying its genomic DNA *in vitro*<sup>8,9</sup>. Unfortunately, *in vitro* amplification regularly fails over large stretches of the genome, reducing the sensitivity of

mutation detection, and errors are frequently incorporated during amplification, diminishing the specificity of subsequent mutation calls<sup>1</sup>. Alternatively, a cell can be clonally expanded in tissue culture, prior to sequencing, to increase genomic starting material<sup>10–13</sup>, but only limited types of primary human cells can sufficiently expand in tissue culture, reducing the scope of this strategy. Here, we combine elements of each strategy, allowing us to genotype melanocytes from normal skin at single-cell resolution.

## Results

### A workflow to genotype individual skin cells

We collected clinically normal skin from 19 sites across 6 donors. Skin biopsies were obtained from cadavers with no history of skin cancer or from peritumoral tissue of donors with skin cancer (Fig. 1a). All donors were of light skin tone, European ancestry (Extended Data Fig. 1a), and ranged from 63 to 85 years in age.

From each skin biopsy, epidermal cells were established in tissue culture for approximately two weeks and subsequently single-cell sorted and clonally expanded. On average, 38% of flow-sorted melanocytes produced colonies, ranging from 2–3000 cells (median 184 cells, Supplementary Table 1), indicating that we are studying a prevalent and representative population. Despite the small size of these colonies, there was sufficient starting material to achieve an allelic dropout rate of only 0.14% (Extended Data Fig. 2a).

Next, we extracted, amplified, and sequenced both DNA and RNA from each clonal expansion, as described<sup>14,15</sup>. Our tissue culture conditions were tailored for melanocyte growth, but some keratinocytes and fibroblasts also grew out. The RNA sequencing data confirmed the identity of each cell (Fig. 1b, Extended Data Fig. 1b–c). The matched DNA/RNA sequencing data also permitted genotype/phenotype inquiries, as described in subsequent sections.

Polymerases often introduce errors during amplification, and these artifacts can be difficult to distinguish from somatic mutations. The matched DNA/RNA sequencing data improved the specificity of mutation calls because mutations in expressed genes could be cross-validated, whereas amplification artifacts arise independently during DNA and RNA amplifications and thus do not overlap (Fig. 1c). To further improve the specificity of mutation calls, we leveraged haplotype information to root out amplification artifacts. When reads are phased into their maternal and paternal haplotypes using heterozygous germline variants, neighboring somatic mutations occur within all amplified copies of that haplotype, whereas amplification artifacts rarely display this pattern (Fig. 1d)<sup>16,17</sup>.

Altogether, we were able to confidently distinguish true somatic mutations from amplification artifacts in portions of the genome that were expressed and/or could be phased. Variants that fell outside of these regions were classified as somatic mutations or artifacts based on their variant allele frequencies. Heterozygous mutations should have allele frequencies of 50%, whereas, amplification artifacts tend to have much lower allele frequencies. For each cell, we identified the variant-allele-frequency cutoff that would maximize the specificity and sensitivity of somatic mutation calls by comparing the variant

allele frequencies of the known somatic mutations and the known amplification artifacts in the expressed and phase-able portions of the genome (Fig. 1e, Extended Data Fig. 2b–d).

To assess the quality of mutation calls, we explored the genomic contexts of somatic mutations and amplification artifacts classified by each of the methods described above (Extended Data Fig. 3). Somatic mutations – whether ascertained by cross-referencing RNA-sequencing data, or from their haplotype distribution, or inferred by their allele frequency – displayed a pattern similar to signature 7, known to be associated with exposure to UV radiation. By contrast, amplification artifacts were more similar to signatures scE and scF, recently defined as likely artifacts resulting from multiple displacement amplification<sup>18</sup>.

Finally, we deduced copy number alterations from both the DNA-seq data and the RNA-seq data using the CNVkit software suite<sup>19,20</sup>. As an additional filter, we required that copy number alterations coincide with a concordant degree of allelic imbalance over the region affected (Fig. 1f).

In summary, we implemented a series of experimental and bioinformatic solutions to overcome the major obstacles associated with genotyping individual melanocytes. 133 melanocytes passed our quality control metrics and were included in all subsequent analyses. Tissue pictures, cellular morphologies, and genomic features are shown for each melanocyte in an extended dataset hosted by figshare (<https://figshare.com/s/bb5614d5ab4554516278>)<sup>21</sup>.

### Mutational landscape of melanocytes from normal skin

For each clone, we performed RNA-sequencing of the entire transcriptome and DNA-sequencing on a panel of 509 cancer-relevant genes (Supplementary Table 2). For a subset of 48 cells we performed an additional round of DNA-sequencing over the entire exome, providing more power to measure the mutational signatures operating in those cells. The mean number of mutations per cell from targeted and whole exome sequencing were respectively 37 and 790 mutations.

We observed an average mutation burden of 7.9mut/Mb (mutations per megabase); however, this ranged from less than 0.82mut/Mb to 32.3mut/Mb, depending upon several factors (Supplementary Table 3). The mutation burdens of melanocytes first varied within people by anatomic site. As expected, melanocytes from sun-shielded sites had fewer mutations than those on sun-exposed sites (Fig. 2a,b and Extended Data Fig. 4). Consistently, sun-shielded melanocytes had little evidence of UV-radiation-induced mutations, whereas, this was the dominant mutational signature in melanocytes from sun-exposed skin (Fig. 2a).

Surprisingly, among sun-exposed melanocytes in this dataset, cells from the back and limbs had more mutations than cells from the face (Fig. 2a,b and Extended Data Fig. 4). Typically, skin from the back and limbs is only exposed intermittently to sunlight and expected to accumulate lower levels of cumulative sun exposure than skin from the face, neck, and bald scalp. The finding of lower mutation burdens in chronically sun-exposed sites deserves further study as it indicates possible differences in mutation rate, DNA repair or turnover among melanocytes from these anatomic sites. However, our observations are consistent

with the fact that melanomas are disproportionately common on intermittently sun-exposed skin as compared to other forms of skin cancer<sup>22,23</sup>.

The mutation burdens of melanocytes also varied between donors. For example, we sequenced melanocytes from a common site, the back, of five donors. Among these, the melanocytes from donors 6 and 13 harbored the highest mutation burdens (Fig. 2c) with more than half of melanocytes exceeding the median mutation burden of melanoma – this was notable because these donors had skin cancer adjacent to the skin that we sequenced.

For several donors, we observed a wide range of mutation burdens among the melanocytes harvested from the same anatomic site. This is surprising as cells originating from the same area of skin (~3cm<sup>2</sup>) would be expected to have similar levels of exposure to UV radiation and therefore comparable mutagenic profiles. To further understand the broad range of mutation burdens, we sought to identify genes whose expression correlates with mutation burden using differential expression analysis (Supplementary Table 4 and Extended Data Fig. 5). Among the significant genes, *MDM2* was more highly expressed in melanocytes with elevated mutation burdens. *MDM2* promotes the rapid degradation of p53, raising the possibility that there is heterogeneity among melanocytes with respect to p53 activity, which could affect the ability of a cell to repair mutations or undergo DNA damage-induced cell death. Although *MDM2* provides a convincing narrative to explain the mutation burden heterogeneity, it is just one out of a number of significantly correlated genes that may be contributing to the phenotype. Another possibility is that the melanocytes may have different residence times in the epidermis. For instance, the low mutation burden melanocytes may reside, or have resided for some portion of their life, in a privileged niche, such as the hair follicle, thereby protecting them from UV-radiation. Future studies will be needed to better resolve why melanocytes from a single site can exhibit such a broad range of mutation burdens.

Melanocytes were harvested near a site with melanoma in two patients, and tumor tissue was available from one of these donors. The mutation burden of the melanoma, determined by bulk sequencing, was comparable to that of the individual melanocytes from its surrounding skin (Fig. 2d). There was no overlap between mutations in the melanoma and surrounding melanocytes, suggesting that few, if any, melanoma cells strayed beyond the excision margins into the normal skin. While more cases need to be studied, our findings suggest that melanomas have mutation burdens similar to their neighboring normal cells. This would contrast with colorectal cancers, which have higher mutation burdens than surrounding normal colorectal cells<sup>24</sup>.

Copy number alterations were relatively uncommon in melanocytes (Fig. 2a middle panel, Extended Data Fig. 6), with the exception of recurrent losses of the Y-chromosome and the inactive X-chromosome (Supplementary Table 5). Mosaic loss of the Y-chromosome and the inactive X-chromosome has been reported in normal blood<sup>25,26</sup>, suggesting that this is a generalized feature of aging. The rarity of autosomal copy number alterations in melanocytes from normal skin is consistent with previous reports that copy number instability is acquired during the later stages of melanoma evolution, and thus unlikely to be operative in pre-neoplastic melanocytes<sup>27,28</sup>.

### Pathogenic mutations in melanocytes from normal skin

We next explored the mutations to identify those that have been previously attributed as drivers of neoplasia. A set of 29 pathogenic mutations were identified in 24 different cells (Table 1). In particular, there were numerous mutations predicted to activate the Mitogen-Activated Protein Kinase (MAPK) pathway. These include loss-of-function mutations in negative regulators of the MAPK pathway, affecting *NFI*, *CBL*, and *RASA2*. There were also gain- or change- of-function mutations in *BRAF*, *NRAS*, and *MAP2K1*, however, *BRAF*<sup>V600E</sup> mutations – the most common mutation in the MAPK pathway occurring in melanocytic neoplasms<sup>29,30</sup> – were not detected.

The World Health Organization (WHO) classification of melanoma distinguishes two major subtypes of cutaneous melanoma – the low cumulative sun damage (low CSD) subtype and the high cumulative sun damage (high CSD) subtype. Low CSD melanomas are driven by *BRAF*<sup>V600E</sup> mutations and often originate from nevi<sup>31</sup>. By contrast, high CSD melanomas are driven by a more diverse set of MAPK-pathway mutations, similar to the ones seen in our study, and they arise *de novo* rather than from nevi<sup>31</sup>. Previous functional studies suggest that the MAPK-pathway mutations in our study are weak activators of the MAPK signaling pathway<sup>32–35</sup>, possibly explaining why they do not give rise to discernible neoplasms by themselves, but they could eventually progress to high CSD melanomas should additional driver mutations arise (Fig. 3).

We also observed driver mutations in other signaling pathways, including mutations that disrupt chromatin remodeling factors and cell-cycle regulators (Table 1). These mutations are presumably not sufficient to induce a neoplasm but likely accelerate progression in the event that the harboring cell acquires a MAPK pathway mutation<sup>36</sup> (Fig. 3). This evolutionary trajectory may explain the evolution of nodular melanoma, a type of melanoma that occurs in the absence of a nevus and grows rapidly<sup>37</sup>.

Interestingly, no *TERT* promoter mutations were found in our study despite their prominence in melanoma<sup>38,39</sup>, suggesting that *TERT* promoter mutations confer little, if any, selective advantage to melanocytes outside of the neoplastic context.

### Melanocytes can persist as fields of related cells within the skin

We found shared mutations between nine separate pairs or trios of melanocytes, suggesting that these cells stem from clonal fields of melanocytes in the skin (Fig. 4 and Extended Data Fig. 7). We ruled out the possibility that these melanocytes emerged during our brief period of tissue culture by growing neonatal melanocytes for several months and measuring their mutation burdens over time (Extended Data Fig. 8). The number of private mutations in the related sets of melanocytes, shown in Figure 4, was many orders of magnitude higher than would be expected from two weeks in tissue culture. Moreover, the private mutations from sun-exposed melanocytes showed evidence of UV-radiation-induced DNA damage (Fig. 4 and Extended Data Fig. 7) – a mutational process that does not operate in tissue culture<sup>18</sup>.

Four of the sets of related melanocytes harbored a pathogenic mutation in the trunk of their phylogenetic trees, implicating the mutation in the establishment of the field. It is possible that the remaining fields of melanocytes had a pathogenic mutation that we did not detect or

appreciate, but we favor the explanation that fields of related melanocytes can also form naturally over time, for instance, as the body surface expands or as part of homeostasis.

## Discussion

There is a complex set of risk factors associated with melanoma, including cumulative levels of sun exposure, peak doses and timings of exposures throughout life, skin complexion, tanning ability, and DNA repair capacity<sup>40</sup>. It is nearly impossible to quantify and integrate the effects of each one of these variables, but we demonstrate here that it is feasible to directly measure the mutational damage in individual melanocytes. Moving forward, the number and types of mutations in melanocytes warrant further exploration as biomarkers to measure cumulative sun damage and melanoma risk.

Our study also offers important insights into the origins of melanoma. Idealized progression models typically depict melanomas as passing through a series of precursor stages, but in reality, most melanomas appear suddenly, without an association to a precursor lesion<sup>41</sup>. We show that human skin is peppered with individual melanocytes or fields of related melanocytes harboring pathogenic mutations known to drive melanoma. These poised melanocytes likely give rise to melanomas that appear in the absence of a pre-existing nevus, once additional mutations are acquired.

Finally, our genomic studies are an important resource to further understand basic melanocyte biology. For example, we found that melanocytes from sun-damaged skin vary in their mutation burdens by multiple orders of magnitude. Of note, a similar pattern of variable mutation burdens was recently reported in bronchial epithelial cells of former smokers<sup>13</sup>. Melanocytes with few mutations are likely to be more efficient at DNA repair and/or have occupied privileged niches, protected from the sun, such as in the hair follicle. Melanocyte stem cells in the hair follicle can contribute to the intraepidermal pool of melanocytes as is evident in vitiligo patients with repigmenting areas<sup>42</sup> – a similar process may be operative in the general population to replenish sun-damaged melanocytes.

In summary, the genetic observations described here offer new insights into the early phases of melanocytic neoplasia, melanocyte homeostasis, and the consequences of UV radiation.

## Methods

### Skin tissue collection

Physiologically normal skin tissue was collected from cadavers (up to 8 days post-mortem) or from surgical discard tissue of living donors. Skin tissue from cadavers was collected from either the UCSF Autopsy program or the UCSF Willed Body Program. Family members consented to donate tissue from the UCSF Autopsy program, and Willed-Body donors consented to donate their tissues for scientific research prior to their expiration. Surgical discard tissue was collected from donors undergoing dermatologic surgery at UCSF, and their consent was obtained at the time of surgery. Donors from the UCSF Willed Body Program have consented to have any data derived from the donation to be deidentified, stored and shared securely, and used for research as required by the Federal Privacy Act of



1974, California Information Practices Act of 1977, and HIPAA (Health Insurance Portability and Accountability Act). Donors from clinical practice have consented to the release and sharing of deidentified clinical data and genetic testing information via HIPAA as guided by the NIH National Human Genome Research Institute. Specifically, the study utilized tissue samples banked under the Pathogen Discovery in Cutaneous Neoplasia/ Cutaneous Neoplasia Tissue Bank protocol (10-01451) at UCSF.

Here, we define physiologically/clinically normal skin as skin lacking palpable or visible lesions. High resolution photos (Nikon D3300 fitted with AF-S DX Micro-NIKKOR 40mm f/2.8G lens) of each skin sample are available in the supplemental dataset. Skin tissue was stored at 4°C and processed in under 24h from time of collection.

### **Establishment of epidermal skin cells in tissue culture**

Skin tissue was briefly sterilized with 70% ethanol and rinsed with Hank's Balanced Salt Solution (Thermo #14175095). Excess dermis was trimmed off and the remaining skin was cut into pieces (approximately 2x2 mm<sup>2</sup>) using surgical scalpel blades. Tissue was incubated in 10mg/ml dispase II (Thermo #17105-041) for 18hr at 4°C. The epidermis was peeled away from the dermis, incubated in 0.5% trypsin-EDTA (Thermo #15400-054) at 37°C for 4 min, and neutralized with 0.5mg/ml soybean trypsin inhibitor (Thermo #17075-029). Epidermal cells were plated in Medium 254 (Thermo #M254500) supplemented with human melanocyte growth supplement-2 (HGMS-2, Thermo #S0165) and antibiotic-antimycotic (Thermo #15240062). Cells were incubated at 37°C, 5% CO<sub>2</sub> for 7–14 days.

### **CRISPR engineering of a subset of cells**

Initially, we presumed that it would be impossible to clonally expand single-cell sorted melanocytes from adult human skin, so we engineered mutations into the *CDKN2A* locus, as described<sup>43</sup>. This decision was based on our previous success in engineering *CDKN2A* mutations into foreskin melanocytes and our ability to clonally expand these melanocytes, thereby producing isogenetic population of engineered melanocytes. However, during the course of these experiments, we recognized that control melanocytes, which were not engineered, could clonally expand under optimized tissue culture conditions, so we subsequently stopped engineering melanocytes. In total, 5 melanocytes were engineered prior to genotyping, as indicated in Supplementary Table 1. Removal of these cell does not affect any of the conclusions from this study.

### **Flow cytometry and cell culture of individual cell clones**

Establishing epidermal cells in tissue culture produced a heterogeneous mixture of cells, comprised primarily of melanocytes and keratinocytes with some fibroblasts present. Differential trypsinization was used to separate melanocytes from keratinocytes using 0.05% trypsin-EDTA (Thermo #25300054) at 37°C for 2 min and 10 min, respectively. Trypsin was neutralized with 0.5mg/ml soybean trypsin inhibitor. Cells were centrifuged at 300 rpm for 5 min, resuspended in 300µl sorting buffer (1X PBS without Ca<sup>2+</sup> and Mg<sup>2+</sup> (Caisson Labs #PBL-01), 1mM EDTA (Thermo #AM9262), 25mM HEPES, pH 7.0 (Thermo #15630130), and 1% bovine serum albumin (Thermo #BP67110)), strained using test tube with 35µm cell strainer snap cap (Corning #352235), and single cell sorted into 96-well plates filled with

100µl complete Medium 254 using a Sony SH800S Cell Sorter. Cell sorting was performed using a 100µm microfluidic sorting chip with the 488nm excitation laser without fluorescent markers.

The next day, cells were screened (Zeiss Axiovert microscope) to decipher their morphology and confirm that each well had only one cell. Individual melanocytes were grown in CnT-40 melanocyte medium (CELLnTEC #CnT-40) supplemented with antibiotic-antimycotic. A small number of cells had keratinocyte or fibroblast morphology. Keratinocytes were grown in 50:50 complete Medium 254 and Keratinocyte-SFM media (Thermo #17005042), and fibroblasts were grown in complete Medium 254 for 10-14 days. After 10-21 days, clone sizes ranged from 2-3000 cells (Supplementary Table 1) and ceased any further expansion, prompting us to harvest these clones at their peak cell count. Approximately 37.5% of flow-sorted cells typically produced colonies, providing evidence that we are studying a prevalent and representative population.

### Extraction and amplification of DNA and RNA from each clone

Clones of 2-3000 cells do not yield enough genomic material to directly sequence using conventional library preparation technologies. For this reason, we elected to isolate both DNA and RNA from each clone and pre-amplify the nucleic acids prior to sequencing. To do this, we utilized the G&T-Seq protocol<sup>14,15</sup>.

G&T-Seq was performed, as described<sup>14,15</sup>. In brief, clones of cells were lysed in 7.5µl RLT Plus Buffer (Qiagen #1053393). mRNA and genomic DNA were separated using a biotinylated oligo d(T)<sub>30</sub> VN mRNA capture primer (5'-biotin-triethyleneglycol-AAGCAGTGGTATCAACGCAGAGTACT30VN-3', where V is either A, C or G, and N is any base; IDT) conjugated to Dynabeads MyOne Streptavidin C1 (Thermo #65001). cDNA was synthesized using the Smart-Seq2 protocol using SuperScript II reverse transcriptase (Thermo #18064014) and template-switching oligo (5'-AAGCAGTGGTATCAACGCAGAGTACrGrG+G-3', where "r" indicates a ribonucleic acid base and "+" indicates a locked nucleic acid base; Qiagen). cDNA was amplified using KAPA HiFi HotStart ReadyMix kit (Roche #KK2502) and purified in a 1:1 volumetric ratio of Agencourt AMPure XP beads (Thermo #A63880). The average yield of amplified cDNA was 305ng. Genomic DNA was purified in a 0:0.72 volumetric ratio of Agencourt AMPure XP beads and amplified using multiple displacement amplification with the REPLI-g Single Cell Kit (Qiagen #150345) to yield an average of 815ng amplified genomic DNA per clone.

### Library preparation and next-generation sequencing of amplified DNA and RNA

We next prepared the amplified cDNA and amplified genomic DNA for sequencing. Library preparation was performed according to the Roche Nimblegen SeqCap EZ Library protocol. In brief, 250ng DNA input was sheared to 200bp using Covaris E220 in a Covaris microtube (Covaris #520077). End repair, A-tailing, adapter ligation (xGen Duel Index UMI adapters; IDT), and library amplification were performed using the KAPA HyperPrep kit (Roche #KK8504) and KAPA Pure Beads (Roche #KK8001). Library quantification was performed using the Qubit dsDNA High Sensitivity kit and quantitative PCR with the KAPA Quantification kit (Roche #KK4854) on a QuantStudio 5 real-time PCR system.

Target enrichment for next-generation sequencing was performed with the UCSF500 Cancer Gene Panel (developed by the UCSF Clinical Cancer Genomics Laboratory; Roche) or the SeqCap EZ Exome + UTR library probes (Roche #06740294001). All cells initially underwent targeted sequencing, and if a cell had a low mutation burden, or if a cell was phylogenetically related to other cells, we sequenced it again with exome baits. The exome sequencing data yielded more mutations, allowing us to infer mutational processes in low mutation burden cells and in distinct branches of phylogenetically related cells.

Hybridization reaction was performed using the SeqCap EZ Hybridization and Wash Kit (Roche #05634253001). xGen Universal blocking oligos (IDT #1075474), human COT 1 DNA (Thermo #15-279-011), and custom xGen Lockdown probes targeting the telomerase reverse transcriptase (*TERT*) promoter (IDT) were additionally added to the hybridization reaction. After library wash and PCR amplification, the captured library was quantified by Qubit and analyzed using the High Sensitivity DNA kit on Agilent's Bioanalyzer 2500.

*TERT* promoter spike-in baits were made with xGen Lockdown probe sequences (2X tiling):

1. /5Biosg/  
GGGCACAGACGCCAGGACCGCGCTTCCCACGTGGCGGAGGGACTGG  
GGACCCGGGACCCGTCCTGCCCTTACCTTCCAGCTCCGCCTCCTC  
CGCGCGGACCCCGCCCGTCCCGAC
2. /5Biosg/  
CCCGTCTGCCCCTTACCTTCCAGCTCCGCCTCCTCCGCGGGACCC  
CGCCCCGTCCCGACCCCTCCCGGGTCCCGGCCAGCCCCCTCCGGGC  
CCTCCCAGCCCCTCCCCTTCCTTT
3. /5Biosg/  
CGACCCCTCCCGGGTCCCGGCCAGCCCCCTCCGGGCCCTCCCAGCC  
CCTCCCCCTCCTTCCGCGGCCCGCCCTCTCCTCGCGGCGGAGTTTC  
AGGCAGCGCTGCGTCCTGCTGCG
4. /5Biosg/  
CTTCCGCGGCCCGCCCTCTCCTCGCGGCGGAGTTTCAGGCAGCGC  
TGCGTCTGCTGCGCACGTGGGAAGCCCTGGCCCCGGCCACCCCCGC  
GATGCCGCGCGCTCCCGCTGCCGA
5. /5Biosg/  
TGCGCACGTGGGAAGCCCTGGCCCCGGCCACCCCCGCGATGCCGCGC  
GCTCCCCGCTGCCGAGCCGTGCGCTCCCTGCTGCGCAGCCACTACCGC  
GAGGTGCTGCCGCTGGCCACGTTTCG

Libraries were sequenced on an Illumina HiSeq 2500 or Novaseq (paired end 100bp or 150bp). On average, we achieved 489-fold unique coverage from targeted sequencing data, 86-fold unique coverage from exome sequencing data, and 7.75 million reads/clone from RNA-sequencing data.

### Calling a preliminary set of variants

Variant call format files for each clone were generated as described<sup>27</sup>. Briefly, Fastq files underwent quality checks using FastQC (v.2.4.1) and were subsequently aligned to the hg19 reference genome using the BWA-MEM algorithm (v0.7.13). BWA-aligned bam files were further groomed and deduplicated using Genome Analysis Toolkit (v2.8) and Picard (v.2.1.1). For each clone, variants were called using Mutect (v3.4.46) by comparing to bulk normal cells from a distant anatomic site. At this stage, the variants were composed primarily of amplification artifacts and somatic mutations. We leveraged the matched DNA/RNA sequencing data and haplotype information, detailed in the subsequent section, to distinguish between these entities.

### Harnessing the matched DNA/RNA sequencing data to remove amplification artifacts

The DNA and RNA from each clone were separately amplified, and consequently, amplification artifacts were unlikely to affect the same genomic coordinates in both the DNA- and RNA- sequencing reads (Fig. 1c). In contrast, somatic mutations should always overlap, assuming there was coverage of the mutant allele in both the DNA- and the RNA-sequencing data. We applied the following criteria to determine whether this assumption could be met.

To begin, we established rates of allelic dropout in our DNA- and RNA- sequencing data. From known heterozygous SNP sites, we empirically deduced that allelic dropout rates were less than 0.15% in our DNA-sequencing data. We achieved low levels of allelic dropout because of our high sequencing coverage, relatively uniform levels of coverage, and low levels of PCR-bias during amplification. Coverage in the RNA-sequencing data was more variable due to differences in gene expression, but from known heterozygous SNP sites, we empirically deduced that 15X coverage was sufficient to sample both alleles at nearly all variant sites. There were a small number of exceptions for which this did not hold true. Truncating mutations (nonsense, splice-site, and frameshift) are prone to nonsense-mediated decay and were commonly undersampled in our RNA-sequencing data relative to the wild-type allele. Also, mutations on the X-chromosome from female donors tended to be in 100% or 0% of RNA-sequencing reads, depending on whether they resided on the active or inactive X-chromosome. Aside from these examples, allelic variation in expression was minimal, particularly for highly expressed genes, as was previously reported<sup>44</sup>.

Based on these observations, a variant was considered a somatic mutation if it was present in both the DNA- and the RNA- sequencing data from the same clone. Conversely, a variant was considered an amplification artifact if the following conditions were met: the variant was present in the DNA-sequencing data but not the RNA-sequencing data, and there was at least 15X coverage in the RNA-sequencing data, and the variant was not truncating or on the X-chromosome. We declined to make a call in either direction for any variant that did not fulfil these conditions.

A limitation to this approach was that some variants did not reside in genes that were expressed. Nevertheless, 11.6% of variants could be classified as either a somatic mutation or amplification artifact by cross-validating the DNA/RNA sequencing data.

## Harnessing haplotype information to remove amplification artifacts

We also used haplotype information to distinguish between somatic mutations and amplification artifacts. Somatic mutations occur in *cis* with nearby germline polymorphisms, and this pattern is preserved during amplification (Fig. 1d). By contrast, amplification artifacts do not occur in complete linkage with nearby germline polymorphisms for the reasons described below (Fig. 1d).

The germline polymorphisms operate like unique molecular barcodes, designating which amplicons descended from each parental allele. The main reason why amplification artifacts are not in complete linkage with nearby polymorphisms is because there are multiple template molecules, associated with each parental allele, from which to amplify, and each template molecule can be amplified more than once – it is unlikely that the exact same mistakes are made during each independent amplification reaction over an error-free template. For example, we sequenced clonal expansions of cells, so each cell provided one molecule of double-stranded DNA from each allele. Furthermore, both strands of DNA are subject to amplification, thereby doubling the number of template molecules relative to the starting cell number. Finally, a single strand of DNA is repeatedly amplified during multiple displacement amplification, further enhancing the number of times an error-free template is utilized during amplification. Amplification artifacts therefore reveal themselves in the sequencing data by not occurring in complete linkage with nearby polymorphisms.

There was an exception for which the pattern described above did not hold true. A copy number gain or copy-number-neutral loss-of-heterozygosity (LOH) results in two or more copies of a single parental allele. If a somatic mutation occurs after the allelic duplication, then the somatic mutation would not be in complete linkage with nearby polymorphisms. Consequently, we did not apply this methodology to root out amplification artifacts over regions of the genome for which there was an allelic duplication.

A limitation to this approach is that we used short-read sequencing technologies, so some variants were too far away from the nearest polymorphic sites to be phased. Nevertheless, 14.7% of variants could be classified as either a somatic mutation or amplification artifact, using the phasing approach.

## Inferring the mutational status of variants outside of the expressed or phase-able portions of the genome

In total, 25.1% of variants could be classified as either a somatic mutation or amplification artifact, using either the expression or the phasing approaches, described above. The remaining variants did not reside in portions of the genome that were sufficiently expressed or close enough to germline polymorphisms to permit phasing. For these variants, we inferred their mutational status from their variant allele frequency.

The majority of somatic mutations in our study were heterozygous, and these mutations, as expected, exhibited a normal distribution of mutant allele frequencies centered at 50% (Fig. 1e, Extended Data Fig. 2b). The standard deviation of mutant allele frequencies in a given clone was dictated primarily by the number of starting cells, indicating that allelic biases, introduced during amplification, were the primary drivers of “noise” in our data.

By contrast, amplification artifacts exhibited a much different distribution of allele frequencies. Most amplification artifacts occurred in later rounds of amplification, and therefore had extremely low variant allele frequencies. However, a small number of amplification artifacts occurred in relatively early rounds of amplification and were disproportionately amplified thereafter. As a result, amplification artifacts exhibited a distribution of allele frequencies with a low peak but a long tail, sometimes extending into the range of allele frequencies seen for somatic mutations (Fig. 1e, Extended Data Fig. 2b). As expected, the tail of this distribution was more extreme in clones with fewer starting cells because amplification biases were more exacerbated in these clones.

Due to the distinct distributions of variant allele frequencies for somatic mutations and amplification artifacts, a variant allele frequency cutoff could distinguish the vast majority of somatic mutations from amplification artifacts. However, the sensitivity and specificity of somatic mutation calls, using this approach, varied for each clone, primarily based on the clone size for the reasons described above. We were able to precisely define the sensitivity and specificity of mutation calls, and we could optimize the VAF cutoff for each clone by studying the overlap in variant allele frequencies from known somatic mutations and known amplification artifacts.

For each clone, we had a set of known somatic mutations and known amplification artifacts, situated in the expressed and phase-able portions of the genome. We were therefore able to determine the proportion of false positives and false negatives under the assumption that all variants above a given variant allele frequency were somatic mutations. Here, a “false positive” is an amplification artifact that would have been called somatic mutations, and a “false negative” is a somatic mutation that would have been called an amplification artifact. We plotted the sensitivity and specificity of mutation calls at different variant allele frequency cutoffs for each clone, and we chose the variant allele frequency cutoff that maximized these values – this value was then applied to the variants whose mutational status was unknown – i.e. the variants outside of the expressed and phase-able portions of the genome. For clones greater than 5 cells, we could typically infer somatic mutations at greater than 98% specificity and 98% sensitivity (Extended Data Fig. 2c,d). We indicate in Supplementary Table 3 whether each mutation was validated or inferred by this approach.

### Copy Number Analysis

Copy number alterations were inferred from both the DNA- and the RNA- sequencing data using CNVkit (v0.9.5.3)<sup>19,20</sup>. We also integrated allelic frequencies from somatic mutations and germline heterozygous SNPs.

First, we inferred copy number alterations from the DNA-sequencing data. CNVkit can be run in reference or reference-free mode. We elected to run CNVkit in reference mode, and in doing so, we created several references, encompassing panels of clones without copy number alterations that were amplified and prepared for sequencing in similar batches. This approach consistently produced the least noisy copy number profiles, as compared to reference-free mode or a universal reference. All other parameters were run on their default settings.

Second, we inferred copy number alterations from the RNA-sequencing data. Briefly, CNVkit assumes the expression of a gene correlates with its copy number status. Of course, the expression of a gene is dictated by several factors, including, but not limited, to copy number. As an input, CNVkit accepts correlation values from an independent dataset between expression and copy number. Here, we included correlation values from the melanoma TCGA project. Given this input, CNVkit downweights genes whose expression does not correlate well with copy number.

Third, we calculated allelic imbalance over germline heterozygous germline SNPs. Copy number alterations are expected to induce imbalances over these sites. Additionally, we calculated the allelic frequencies of somatic mutations across the genome, as these, too, would be modulated by copy number alterations.

Finally, we manually reviewed the copy number and variant allele information to call copy number alterations that were supported by each approach.

### Establishing cell identity

We made morphologic predictions when screening single cell clones of melanocytes, fibroblasts, and keratinocytes to designate cell identity. Melanocytes have a cell body with stellar or dendritic projections, are darker due the presence of melanin, and tend to grow in tighter clusters than fibroblasts, albeit not as tight as keratinocytes. Keratinocytes have a polygonal cell shape with more regular dimensions and grow in a very tight cluster due to the presence of desmosomes. Fibroblasts are flat, oblong or triangular shaped cells that divide very quickly in a diffuse cluster as a characteristic meshwork. In addition to cell morphology, we inspected the gene expression of *MLANA*, *TYR*, *PMEL*, and *S100B*. The protein products of these genes are well-established markers of the melanocyte cell lineage and are commonly used in the clinical setting to distinguish melanocytes and tumors of melanocytic origin from other cell lineages and other tumor types. There was a clear separation of gene expression levels of these genes between the cells that we nominated as melanocytes versus keratinocytes/fibroblasts (Extended Data Figure 1c).

### An overview of the genetic landscape of each sequenced melanocyte

We have included individual summaries of the 133 sequenced clones which describes cellular morphology and tissue images, validation of variant allele fraction of raw calls, copy number alterations, and *CDKN2A* status (where applicable) (<https://figshare.com/s/bb5614d5ab4554516278>).

### Admixture Analysis (related to Extended Data Figure 1a)

Bulk normal cells were analyzed to identify germline variants present in each studied donor. Donor ethnicity was inferred via Admixture analysis using a Bayesian modelling approach employed by the tool STRUCTURE (v2.3.4)<sup>45</sup>. A set of 7662 common variants (1000 genomes population allele frequency > 0.05) with a sequencing depth of greater than 10 across all donors and all 2504 samples from the 1000 genomes study<sup>46</sup> were selected. The burn-in period and analysis period were both completed with 10,000 repetitions as per the tool recommendations to achieve accurate estimations of admixture. To select an appropriate

number of populations ( $K$ ), the algorithm was run using  $K$  estimations of 5 to 9. A final  $K$  value of 8 was selected to appropriately cluster populations without overfitting. The data were plotted using the STRUCTURE GUI plotting tool. Ethnicity of donors within this study was inferred by their similarity to known populations within the 1000 genomes set<sup>46</sup>.

### **RNA gene expression analysis (related to Figure 1b and Extended Data Figure 1b)**

RNA sequencing reads were aligned to the transcriptome as well as the hg19 reference genome using STAR alignment tool (v2.5.1b)<sup>47</sup>. Transcripts were quantified using RNA-Seq by Expectation-Maximization (RSEM) (v1.2.0)<sup>48</sup> and filtered to remove those with fewer than 10 reads across all clones as recommended by DESeq2 R package documentation. A variance stabilizing transformation was applied to the data and a Barnes-Hut T-distributed stochastic neighbour embedding (t-SNE) algorithm was performed to cluster related cells on the expression of the top 500 genes using the Rtsne R package (v0.15) with a perplexity of 6 over 1000 iterations.

Differential expression analysis was completed on the quantified transcript values using DESeq2 R package<sup>49</sup> (v1.22.2). Three experimental designs were produced, selecting for differentially expressed genes that are over-expressed in fibroblasts, melanocytes, and keratinocytes independently. The data were  $\log_2$  transformed and a heatmap was generated presenting the top 20 significantly differentially over-expressed genes per cell type.

Gene set enrichment analysis was performed across the significantly differentially over-expressed genes from each cell type using the Molecular Signatures Database (v6.2) webtool. The top significantly enriched pathways were examined for their relation to the cell-type of interest.

### **Mutation burden and signature analysis (related to Figure 2)**

The mutation burdens reported in Figure 2 correspond to the number of somatic mutations in a given clone divided by the genomic footprint for which mutations could be detected. Due to differences in depth of coverage across bam files and the unevenness of coverage in a given bam file, mutations were not callable at every base present in target region. Additionally, we used both a targeted and exome sequencing panel in this study, which produce two different sequencing footprint sizes. To account for these issues, we calculated callable sequencing footprints for each clone and corresponding reference. On-target bam files were created per clone and per bulk normal. The coverage of each on-target base was calculated using the bedtools (v2.25.0) `genomcov` command, and the number of bases covered by more than 5 reads was counted in each bam file. The minimum value between a clone's bam and its reference bam was used as the footprint from which to calculate a mutation burden for each clone.

Linear mixed-effect models were generated using the `lmer` library in R to identify any association between sun-exposure (as determined by the anatomic site from which the single cell was derived) and mutation burden while correcting for the donor of origin. P values of each pairwise comparison derived from this model with the `lmer` package are shown in figure 2b. To further account for the repeated measurements per donor, a model was created



excluding the sun-exposure variable and an ANOVA was performed comparing the fit of the two models.

To perform mutational signature analysis, surrounding genomic contexts were applied to single nucleotide variants identified in each clone using the Biostrings hg19 human genome sequence package (BSgenome.Hsapiens.UCSC.hg19 v1.4.0). Variant contexts were used to assess the proportion of each clone's mutational landscape that could be attributed to a mutagenic process using the deconstructSigs R package (v1.8.0). A set of 48 signatures recently described by Petljak *et al*<sup>18</sup> were analysed, with particular attention paid to the single base substitution signatures 7a, 7b, and 7c that are associated with ultraviolet light exposure.

### Identifying Pathogenic Mutations (related Table 1)

Here, we define a pathogenic mutation to be a mutation that is under positive selection in cancer.

To identify gain- or change- of-function mutations affecting oncogenes, we interrogated whether the mutations in our study overlapped with previously defined mutational hotspots. First, we referenced the COSMIC database (see column M "COSMIC\_ID" of Supplementary Table 3). There are thousands of entries in the COSMIC database, so mutations could recur at low frequency at certain positions by chance alone. Therefore, we curated these mutations to identify those with a previously published biological function. From this analysis, we identified hotspot mutations affecting *BRAF*, *NRAS*, *MAP2K1*, *CBL*, and *PPP6C* (detailed in Table 1). In parallel, we referenced [cancerhotspot.org](http://cancerhotspot.org), a curated database of mutational hotspots. From this analysis, we corroborated the hotspot mutations affecting *BRAF*, *NRAS*, *MAP2K1*, and *PPP6C*. In addition, we found an E548K substitution affecting *PTPRT*. Upon further review, we concluded that the *PTPRT* mutation was unlikely to be biologically active because the gene is not expressed in the melanocytic cell lineage and the mutations in this gene do not show evidence of positive selection in melanoma<sup>50</sup>, and therefore we elected not to highlight this gene in our analysis.

To identify loss-of-function mutations affecting defined tumor suppressor genes in our study, we referred to previous melanoma publications<sup>33,50</sup>. From this analysis, we identified mutations affecting *NF1*, *CBL*, *RASA2*, *CDKN2A*, *ARID2*, *PTEN*, and *DDX3X*. There were also mutations affecting genes that are likely tumor suppressors in melanoma but have yet to be unequivocally defined as such. We elected not to highlight these mutations in Table 1; however, we encourage readers to consult the full list of mutations in Supplementary Table 3, as the number of pathogenic mutations likely exceeds the more conservative assessment shown in Table 1.

### Gene expression correlation with mutation burden (related to Supplementary Table 4 and Extended Data Figure 5)

RNA data was used to explore the variability in mutation burdens, often observed over a single site. Sites with greater than 3 standard deviations of mutation burdens, demonstrating the presence of both high and low mutation burden clones, were selected for analysis. Mutation burdens were normalized to the median of each anatomic site. Differential

expression analysis was then performed using DESeq2 R package<sup>49</sup> (v1.22.2). Genes with expression changes significantly associated (adjusted p value < 0.01) with a continuous change in mutation burden are highlighted in Supplementary Table 4 and Extended Data Fig. 5.

### **Estimating mutation acquisition over time in tissue culture (related to Extended Data Fig. 8)**

We established skin cells in tissue culture for 7-14 days prior to single-cell sorting and clonal expansion. Any mutation that arose after clonal expansion would be recognizable since it would only be present in a proportion of daughter cells, thus appearing subclonal. However, mutations that arose during the brief period of tissue culture preceding clonal expansion could be mistaken as a mutation that occurred while the cell was still situated in the skin. We therefore sought to establish the rate at which melanocytes accumulate *de novo* mutations in tissue culture to determine whether this was a meaningful contribution to the total mutation burden that we observed in our cells.

Towards this goal, we followed the framework recently put forth by Petljak and colleagues<sup>18</sup> – in that study, the authors sequenced subclones of daughter cells from common cancer lines at different generational time points for up to 161 days, thereby revealing the mutational processes operating during their time in tissue culture. Here, we sequenced a bulk culture of normal human melanocytes derived from human foreskin to establish the germline variants and somatic mutations in the dominant clones. We continued to culture these cells, and at time points of 51, 63, 120, and 239 days, we single-cell sorted and clonally expanded individual cells. We genotyped each clonal expansion, following the same protocol that was applied to melanocytes in this study. From these analyses, we estimate that mutations occur at a rate of .045 mutations/Mb per 7 days in tissue culture. To put this in perspective, the mutation burden of melanocytes from the bottom of the foot was .25 mutations/Mb. Based on these findings, we conclude that the number of mutations accumulated in tissue culture was negligible as compared to the number of mutations that pre-existed in melanocytes that were profiled for this study.

We also analyzed the publicly available data from Petljak *et al*<sup>18</sup> to deduce the rate at which melanoma cell lines accumulate mutations in tissue culture. From these analyses we estimate that mutations occur at a rate of .043 mutations/Mb per 7 days – in line with our estimates for normal human melanocytes.

Taken together, it is not surprising that the number of mutations collected from 7 days in tissue culture is negligible as compared to the number of mutations collected from decades situated in the skin.

### **Phylogenetic tree construction (related to Figure 4 and Extended Data Fig. 7)**

Pairwise comparisons of melanocyte mutation calls were performed to identify sets of melanocytes with shared mutations, and when this occurred, phylogenetic trees were constructed from the shared and unshared mutations. In Figure 4, trunk lengths correspond to the number of shared mutations, and branch lengths correspond to the number of unshared mutations. If there was an allelic deletion in one clone, we did not assign mutations in the

clone lacking the deletion over the deletion area to the branch. Shared mutations were discarded if there was insufficient coverage in the reference to rule out the possibility that the mutation was a germline SNP. Unshared mutations were discarded if sequencing coverage was insufficient in one clone to definitively make a call. In practice, few mutations needed to be discarded by these filtering criteria because we achieved high sequencing coverage in our clones.

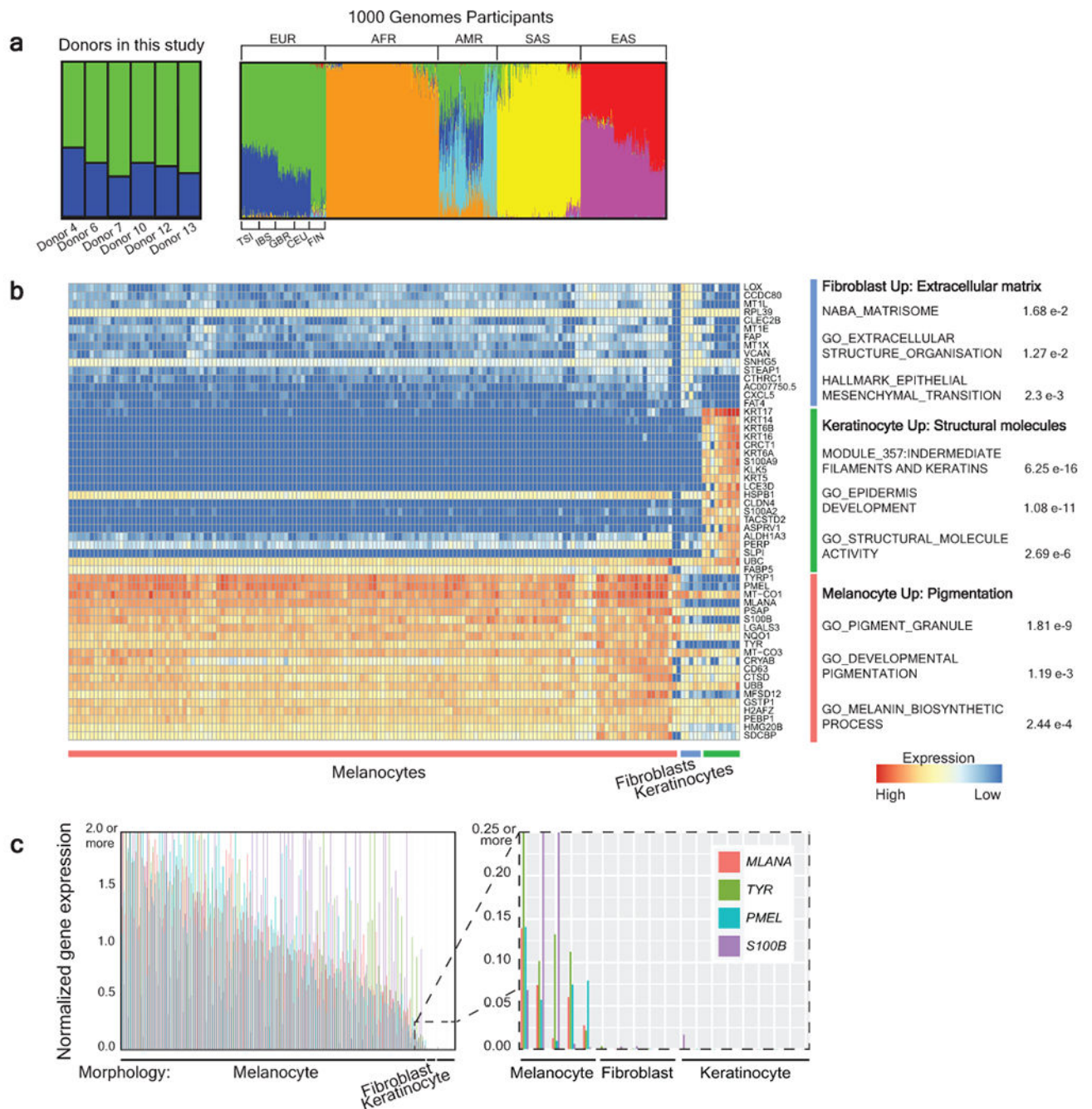
Author Manuscript

Author Manuscript

Author Manuscript

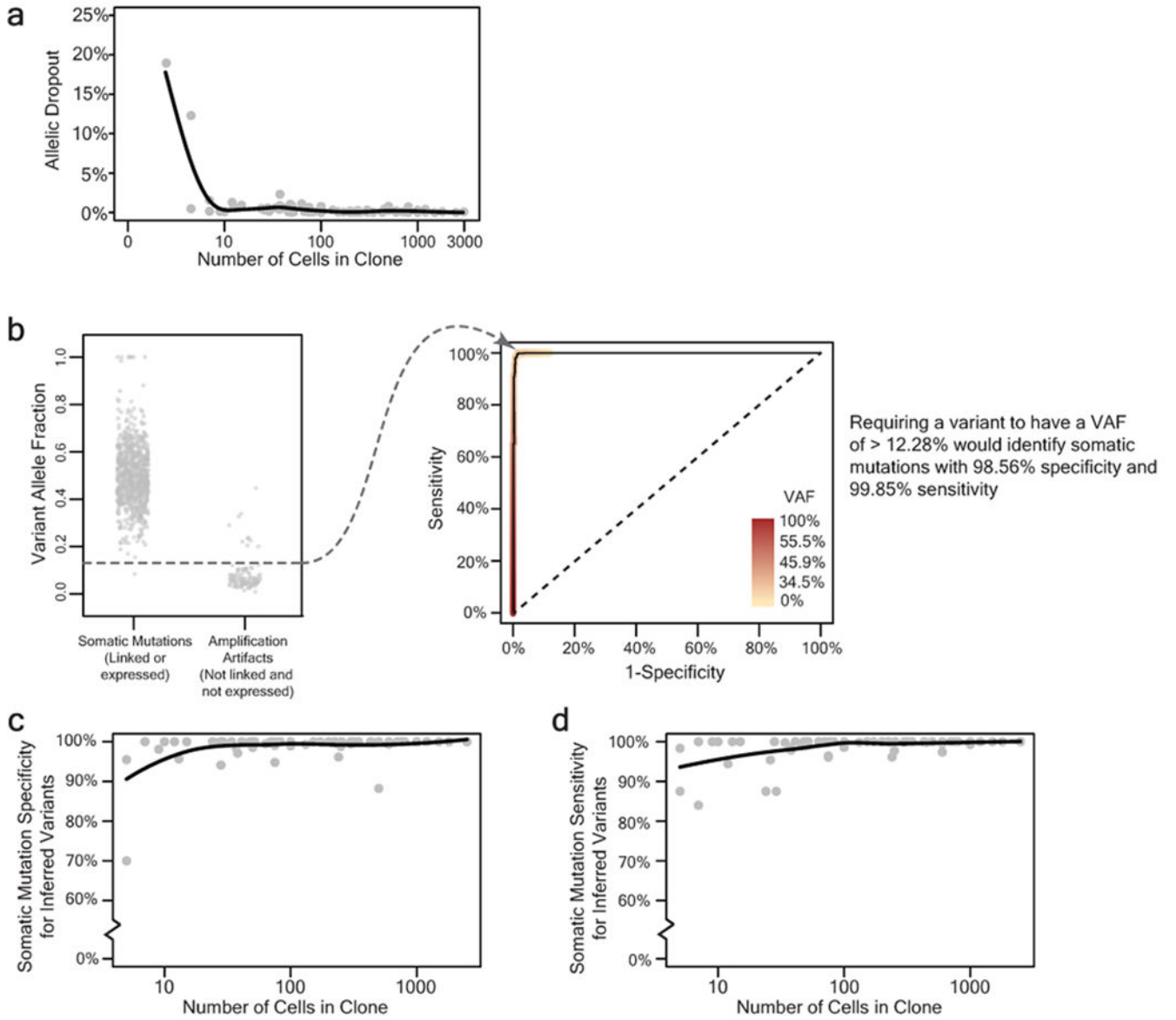
Author Manuscript

## Extended Data



**Extended Data Figure 1 | Establishing the ethnicity of donors and identity of cells in this study.**  
**a**, Admixture analysis of donors included in this study alongside participants from the 1000 Genomes Project. Donors in our study were genotypically most similar to European participants from the 1000 Genomes Project. EUR- European (TSI-Toscani in Italia, IBS - Iberian Population in Spain, GBR - British in England and Scotland, CEU - Utah Residents with Northern and Western European Ancestry, FIN - Finnish in Finland), AFR - African,

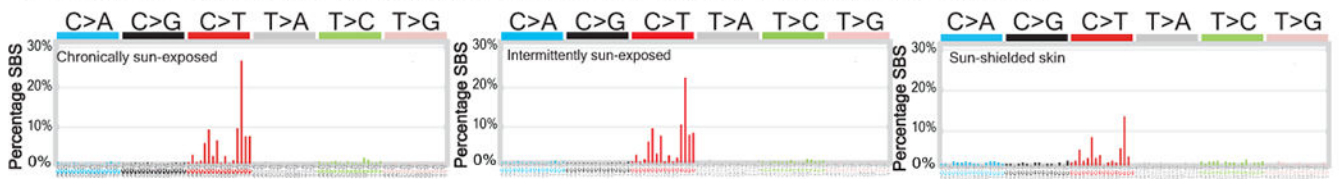
AMR - Latin American, SAS - South Asian, and EAS - East Asian. **b**, Differential expression analysis comparing cells that were morphologically predicted to be keratinocytes, melanocytes, or fibroblasts (see Fig. 1B for more details). The top 20 differentially expressed genes for each group are shown along with gene ontology terms with significant overlap. **c**, Cells with melanocyte morphology express higher levels of known melanocyte markers. Bar plots showing gene expression levels of *MLANA*, *TYR*, *PMEL*, and *S100B*, colored as indicated. A value of 1 is equivalent to the medium FPKM value for that gene across cells. Each quartet of bars corresponds to an individual clone, and clones are rank ordered by their medium normalized gene expression values for these 4 genes. The zoomed inset portrays the 5 melanocyte clones with lowest expression levels of melanocyte markers adjacent to the fibroblast and keratinocyte clones.



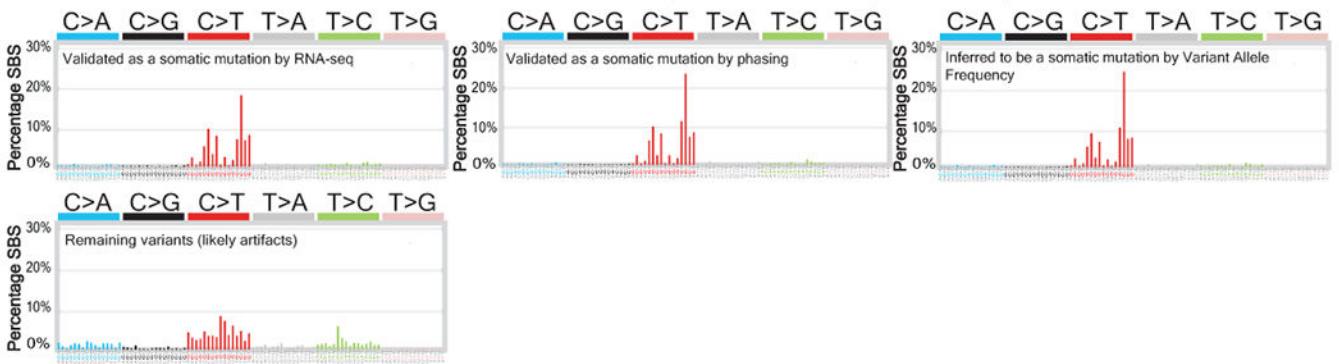
**Extended Data Figure 2 |. Detection of somatic mutations in small clones of skin cells with high specificity and sensitivity.**

**a**, Allelic dropout declines rapidly as a function of clone size. Each data point represents the percent of germline SNP alleles that could not be detected for a given clone as a function of the number of cells within the clone. **b**, Establishing a variant allele fraction (VAF) cut-off to infer somatic mutations within a clone. The left panel depicts the VAFs for known somatic mutations and known amplification artifacts from a single clone. The right panel depicts a ROC curve, showing the VAF at which sensitivity and specificity of somatic mutation calls would be maximized when inferring the mutational status of variants based on VAF alone. Variants that fell within expressed or phase-able portions of the genome were classified as mutations or artifacts as described (see Fig. 1c, d). The remaining variants were inferred based on the VAF cut-off, which maximized sensitivity and specificity of somatic mutation calls. **c-d**, The specificity (panel c), and sensitivity (panel d), of inferred somatic mutations as a function of clone size. The mean specificity and sensitivity of inferred somatic mutations was respectively 98.83% and 98.60% for all clones of at least 5 cells. All trendlines correspond to a moving average.

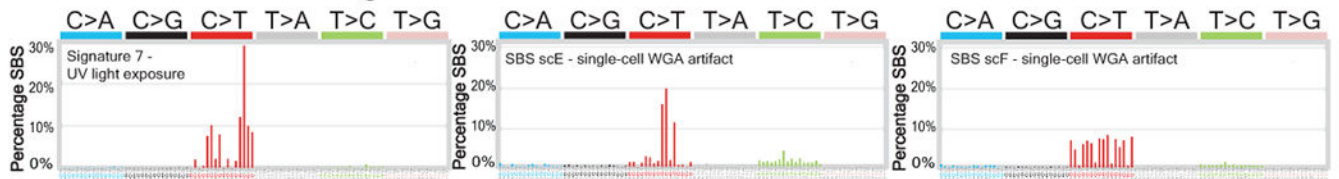
**a Contexts of somatic mutations identified in skin of varying sun exposure**



**b Contexts of substitutions identified in sun-exposed skin, organised by validation status**

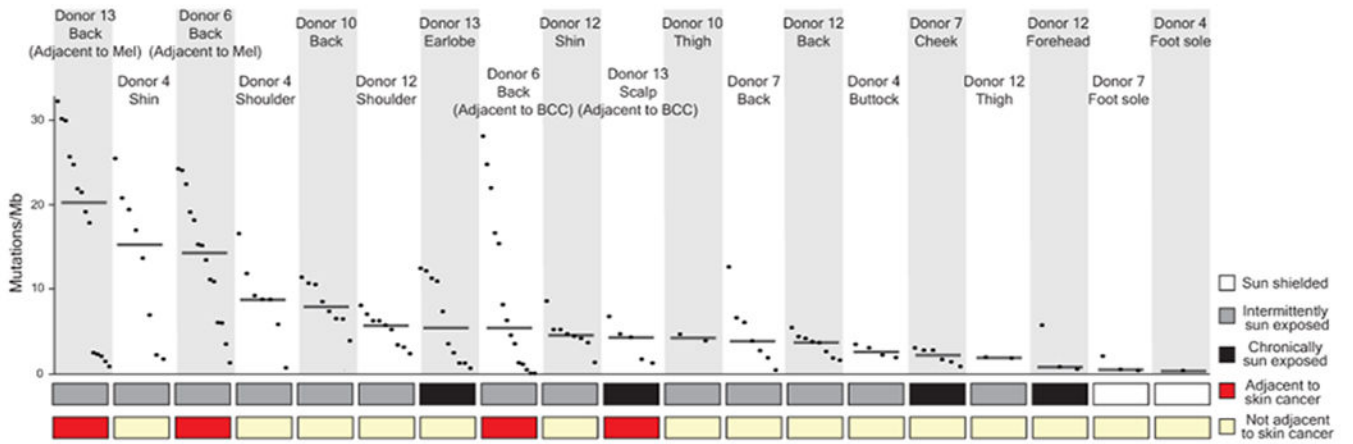


**c Predefined mutation signatures**

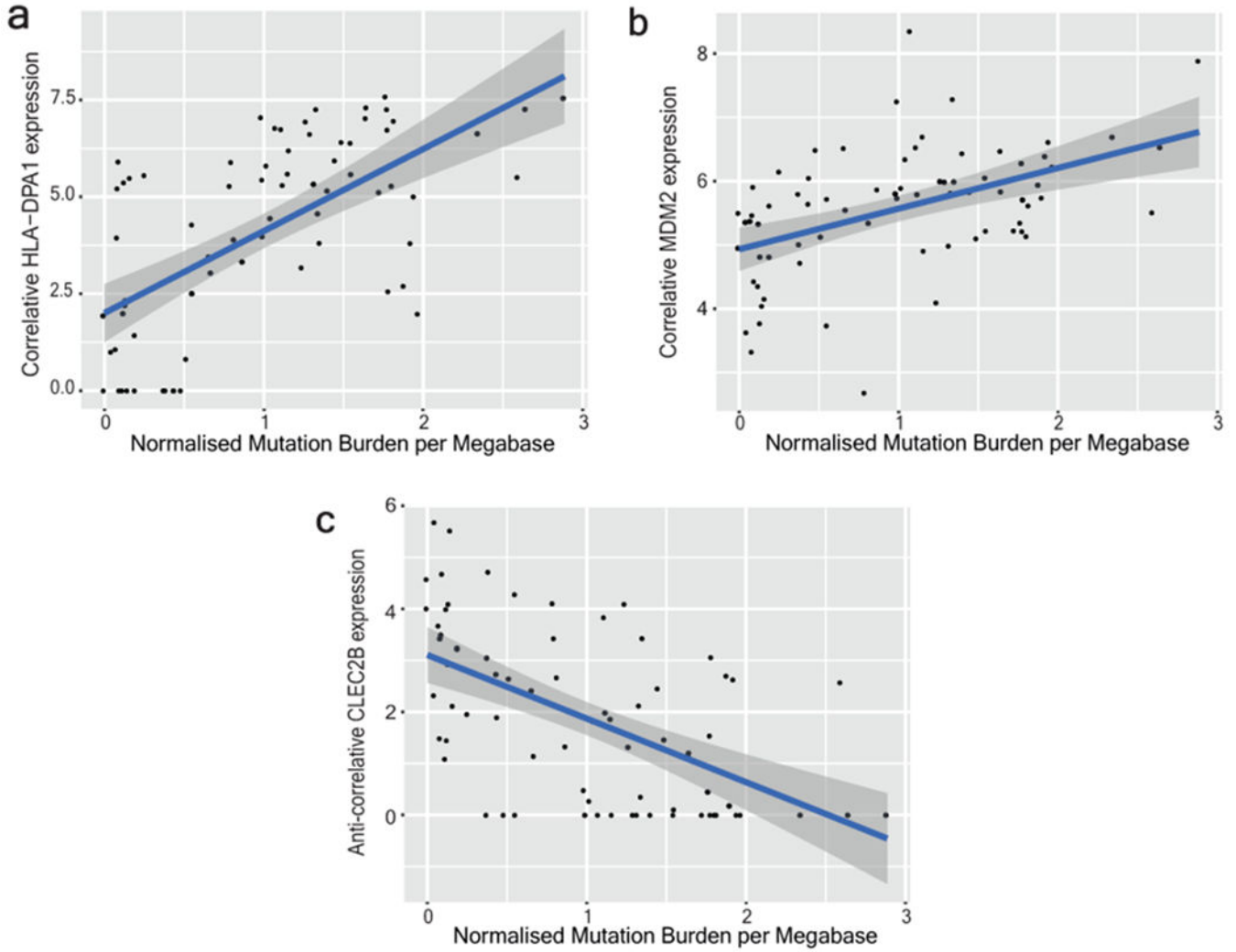


**Extended Data Figure 3 |. Contexts of single-base substitutions corroborate the quality of somatic mutation calls.**

**a**, The proportion of somatic mutations identified in chronically sun-exposed, intermittently sun-exposed, and sun-shielded skin that belong to each of the 96 trinucleotide substitution contexts. Note the similarity to signature 7 (shown for reference in panel c), albeit to a lesser extent in sun-shielded skin cells. **b**, Tri-nucleotide contexts of variants from sun-exposed skin validated to be somatic mutations by RNA-seq or phasing as well as variants inferred to be somatic mutations by their variant allele frequency (VAF). Note the similarity to signature 7. The tri-nucleotide contexts of remaining variants (assumed to be amplification artifacts) are also shown. **c**, Predefined mutation signatures shown for reference; Signature 7 (associated with UV-radiation-induced DNA damage)<sup>51</sup>, and SBS scE and SBS scF, which are associated with single-cell whole genome amplification artifacts<sup>18</sup>.



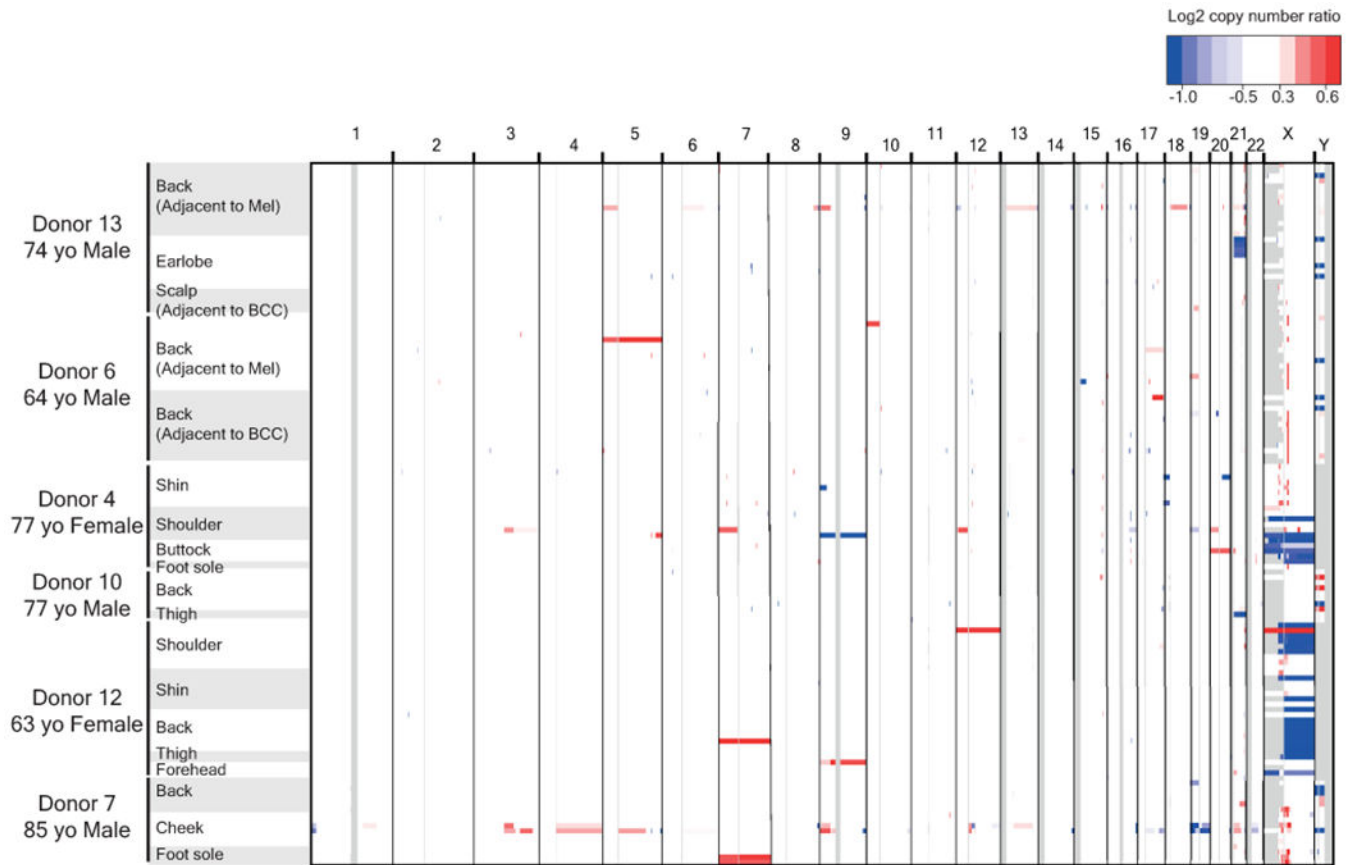
**Extended Data Figure 4 |. Median mutation burden of melanocytes from different anatomic sites.** Mutation burden of melanocytes from physiologically normal skin of six donors across different anatomic sites with varied sun exposure that are rank ordered by median mutation burden (line) within each site. (BCC = Basal Cell Carcinoma, Mel = Melanoma)



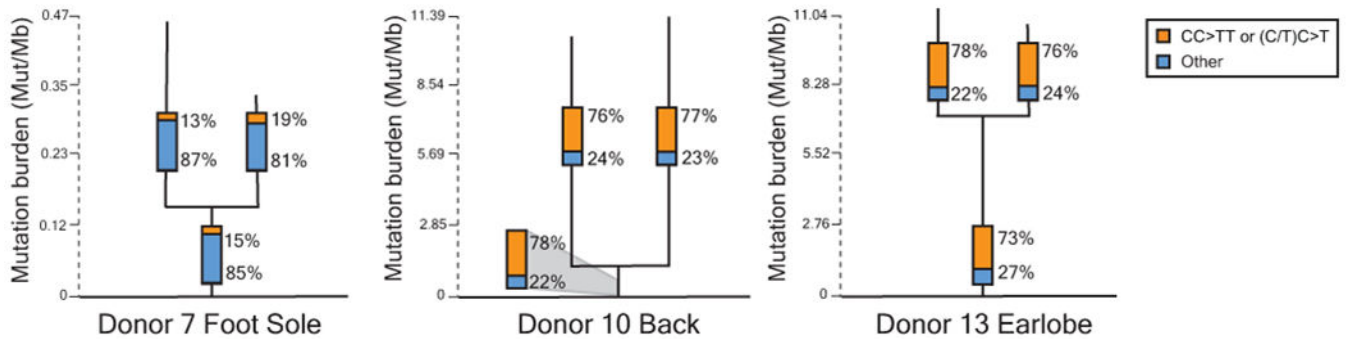
**Extended Data Figure 5 | Differential expression analysis revealing genes significantly correlating with mutation burden.**

**a-c,** Gene expression versus normalised mutation burden is shown for two top correlative genes (*HLA-DPA1* and *MDM2*) and one (*CLEC2B*) anti-correlative gene of interest from Supplementary Table 4. Clones included in this analysis are from anatomic sites with greater than 3 standard deviations of mutation burdens among their cells, thus demonstrating a range of mutation burdens. The plotted blue line represents a linear model fit to the data with 95% confidence intervals for that model prediction shown in grey.





**Extended Data Figure 6 |. Copy number landscape of melanocytes from normal human skin.** Copy number was inferred, as described, and segments (regions of equal copy number) are depicted, here, denoting gains (red) and losses (blue) for each melanocyte (rows). Note that copy number alterations over autosomes were rare, whilst the loss of one sex chromosome is a common occurrence. All X chromosome deletions in females affect the inactive X (see Supplementary Table 5).

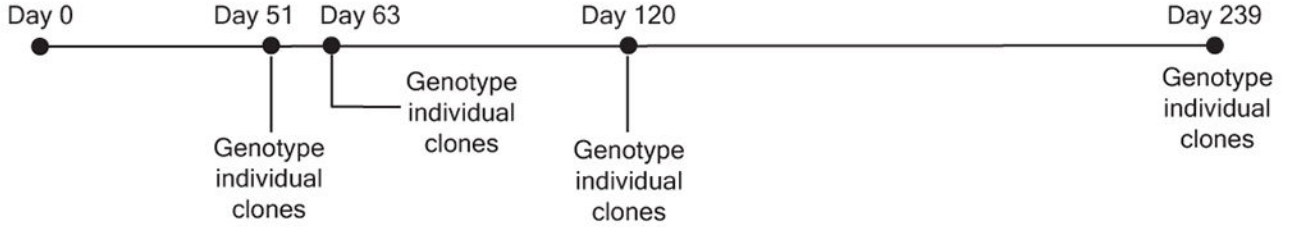


**Extended Data Figure 7 |. Fields of related melanocytes exist within the skin.** Phylogenetic trees in which each branch corresponds to an individual cell. Mutations that are shared between cells comprise the trunk of each tree and private mutations in each cell form the branches. Trunk and branch lengths are scaled equivalently within each tree but not

across trees. The proportion of mutations that can be attributed to ultraviolet radiation (CC>TT or (C/T)C>T) is annotated in the bar charts on each tree trunk or branch.

**a**

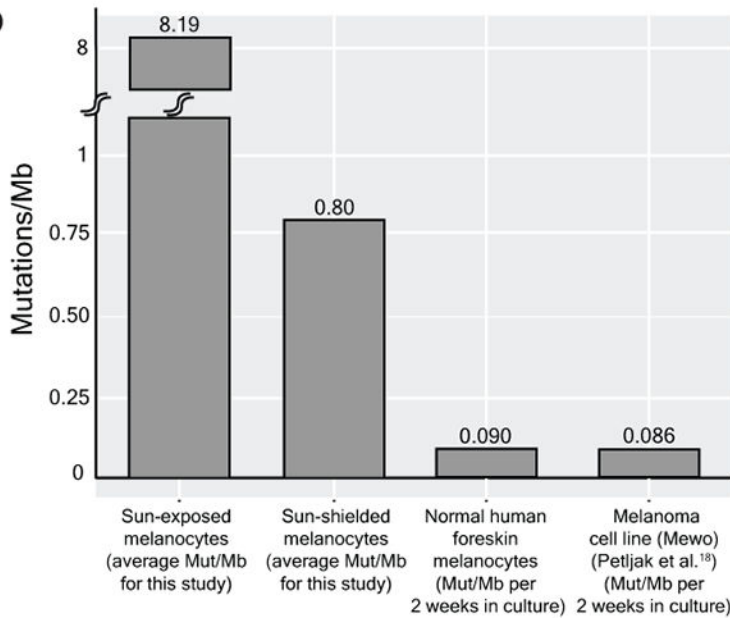
Timeline of normal human melanocytes in culture



Timeline of Mewo cutaneous melanoma cell line in culture (Petljak et al<sup>18</sup>)



**b**



**Extended Data Figure 8 | Melanocytes accumulate few mutations in tissue culture.**

**a**, We sequenced a bulk culture of neonatal melanocytes to establish the germline SNPs and somatic mutations in the dominant clones. We continued to passage the cell line for 239 days, genotyping individual clones at the timepoints indicated to establish the rate at which mutations were acquired in culture. In parallel, Petljak et al<sup>18</sup> performed similar experiments on common cancer cell lines, and we analysed their data from a melanoma cell line (Mewo) included in their study. **b**, On average, the mutation burden of neonatal melanocytes and

Mewo cells respectively increased by 0.090 and 0.086 mutations/Mb for every 2 weeks in tissue culture (we typically cultured melanocytes 2 weeks or less in this study). To put these mutation burdens in perspective, the average mutation burdens of sun-exposed and sun-shielded melanocytes from this study are shown in comparison. Based on these results, we conclude that the brief period of tissue culture contributed little towards the mutation burdens observed in our study.

## Supplementary Material

Refer to Web version on PubMed Central for supplementary material.

## Acknowledgements

We acknowledge support from the following: National Cancer Institute – K22 CA217997 (AHS), Melanoma Research Alliance (AHS), LEO Foundation (AHS), George and Judy Marcus Precision Medicine Fund (AHS and STA), National Center for Advancing Translational Sciences and the National Institutes of Health through UCSF-CTSI TL1-TR001871 (JT), 1R35CA220481 (BCB), Mt. Zion Health Research Fund (AHS), Dermatology Foundation (AHS), the American Federation of Aging Research (AHS), and the NIH Director's Common Fund – DP5 OD019787 (RLJ). We thank the tissue donors, whose tissue was obtained through the UCSF Willd Body Program for medical education, and patients who consented to donate surgical discard tissue. Cell sorting was performed in the Laboratory for Cell Analysis of UCSF's Helen Diller Family Comprehensive Cancer Center which is supported by a National Cancer Institute Cancer Center Support Grant (P30 CA082103).

## References

1. Gawad C, Koh W, Quake SR. Single-cell genome sequencing: current state of the science. *Nat Rev Genet* 2016;17(3):175–88. [PubMed: 26806412]
2. Ziegler A, Jonason AS, Leffell DJ, et al. Sunburn and p53 in the onset of skin cancer. *Nature* 1994;372(6508):773–6. [PubMed: 7997263]
3. Jonason AS, Kunala S, Price GJ, et al. Frequent clones of p53-mutated keratinocytes in normal human skin. *Proc Natl Acad Sci USA* 1996;93(24):14025–9. [PubMed: 8943054]
4. Martincorena I, Roshan A, Gerstung M, et al. Tumor evolution. High burden and pervasive positive selection of somatic mutations in normal human skin. *Science* 2015;348(6237):880–6. [PubMed: 25999502]
5. Jaiswal S, Fontanillas P, Flannick J, et al. Age-related clonal hematopoiesis associated with adverse outcomes. *N Engl J Med* 2014;371(26):2488–98. [PubMed: 25426837]
6. Martincorena I, Fowler JC, Wabik A, et al. Somatic mutant clones colonize the human esophagus with age. *Science* 2018;
7. Lee-Six H, Olafsson S, Ellis P, et al. The landscape of somatic mutation in normal colorectal epithelial cells. *Nature* 2019;574(7779):532–7. [PubMed: 31645730]
8. Hou Y, Song L, Zhu P, et al. Single-cell exome sequencing and monoclonal evolution of a JAK2-negative myeloproliferative neoplasm. *Cell* 2012;148(5):873–85. [PubMed: 22385957]
9. Xu X, Hou Y, Yin X, et al. Single-cell exome sequencing reveals single-nucleotide mutation characteristics of a kidney tumor. *Cell* 2012;148(5):886–95. [PubMed: 22385958]
10. Behjati S, Huch M, van Boxtel R, et al. Genome sequencing of normal cells reveals developmental lineages and mutational processes. *Nature* 2014;513(7518):422–5. [PubMed: 25043003]
11. Blokzijl F, de Ligt J, Jager M, et al. Tissue-specific mutation accumulation in human adult stem cells during life. *Nature* 2016;538(7624):260–4. [PubMed: 27698416]
12. Kucab JE, Zou X, Morganella S, et al. A Compendium of Mutational Signatures of Environmental Agents. *Cell* 2019;177(4):821–836.e16. [PubMed: 30982602]
13. Yoshida K, Gowers KHC, Lee-Six H, et al. Tobacco smoking and somatic mutations in human bronchial epithelium. *Nature* 2020;

14. Macaulay IC, Teng MJ, Haerty W, Kumar P, Ponting CP, Voet T. Separation and parallel sequencing of the genomes and transcriptomes of single cells using G&T-seq. *Nat Protoc* 2016;11(11):2081–103. [PubMed: 27685099]
15. Macaulay IC, Haerty W, Kumar P, et al. G&T-seq: parallel sequencing of single-cell genomes and transcriptomes. *Nat Methods* 2015;12(6):519–22. [PubMed: 25915121]
16. Lodato MA, Rodin RE, Bohrson CL, et al. Aging and neurodegeneration are associated with increased mutations in single human neurons. *Science* 2018;359(6375):555–9. [PubMed: 29217584]
17. Bohrson CL, Barton AR, Lodato MA, et al. Linked-read analysis identifies mutations in single-cell DNA-sequencing data. *Nat Genet* 2019;51(4):749–54. [PubMed: 30886424]
18. Petljak M, Alexandrov LB, Brammell JS, et al. Characterizing Mutational Signatures in Human Cancer Cell Lines Reveals Episodic APOBEC Mutagenesis. *Cell* 2019;176(6):1282–1294.e20. [PubMed: 30849372]
19. Talevich E, Shain AH, Botton T, Bastian BC. CNVkit: Genome-Wide Copy Number Detection and Visualization from Targeted DNA Sequencing. *PLoS Comput Biol* 2016;12(4):e1004873. [PubMed: 27100738]
20. Talevich E, Shain AH. CNVkit-RNA: Copy number inference from RNA-Sequencing data. *bioRxiv* 2018;408534.
21. Fewings E, Tang J, Chang D, Shain AH. Genomic landscape of 133 melanocytes from human skin [Internet] [cited 2020 Feb 4]; Available from: <https://figshare.com/s/bb5614d5ab4554516278>
22. Elwood JM, Gallagher RP. Body site distribution of cutaneous malignant melanoma in relationship to patterns of sun exposure. *Int J Cancer* 1998;78(3):276–80. [PubMed: 9766557]
23. Nehal KS, Bichakjian CK. Update on Keratinocyte Carcinomas. *N Engl J Med* 2018;379(4):363–74. [PubMed: 30044931]
24. Roerink SF, Sasaki N, Lee-Six H, et al. Intra-tumour diversification in colorectal cancer at the single-cell level. *Nature* 2018;556(7702):457–62. [PubMed: 29643510]
25. Machiela MJ, Zhou W, Karlins E, et al. Female chromosome X mosaicism is age-related and preferentially affects the inactivated X chromosome. *Nat Commun* 2016;7:11843. [PubMed: 27291797]
26. Forsberg LA, Rasi C, Malmqvist N, et al. Mosaic loss of chromosome Y in peripheral blood is associated with shorter survival and higher risk of cancer. *Nat Genet* 2014;46(6):624–8. [PubMed: 24777449]
27. Shain AH, Joseph NM, Yu R, et al. Genomic and Transcriptomic Analysis Reveals Incremental Disruption of Key Signaling Pathways during Melanoma Evolution. *Cancer Cell* 2018;34(1):45–55.e4. [PubMed: 29990500]
28. Bastian BC, Olshen AB, LeBoit PE, Pinkel D. Classifying Melanocytic Tumors Based on DNA Copy Number Changes. *Am J Pathol* 2003;163(5):1765–70. [PubMed: 14578177]
29. Hodis E, Watson IR, Kryukov GV, et al. A Landscape of Driver Mutations in Melanoma. *Cell* 2012;150(2):251–63. [PubMed: 22817889]
30. Pollock PM, Harper UL, Hansen KS, et al. High frequency of BRAF mutations in nevi. *Nat Genet* 2003;33(1):19–20. [PubMed: 12447372]
31. Shain AH, Bastian BC. From melanocytes to melanomas. *Nat Rev Cancer* 2016;16(6):345–58. [PubMed: 27125352]
32. Yao Z, Yaeger R, Rodrik-Outmezguine VS, et al. Tumours with class 3 BRAF mutants are sensitive to the inhibition of activated RAS. *Nature* 2017;548(7666):234–8. [PubMed: 28783719]
33. Krauthammer M, Kong Y, Bacchiocchi A, et al. Exome sequencing identifies recurrent mutations in NF1 and RASopathy genes in sun-exposed melanomas. *Nat Genet* 2015;
34. Grand FH, Hidalgo-Curtis CE, Ernst T, et al. Frequent CBL mutations associated with 11q acquired uniparental disomy in myeloproliferative neoplasms. *Blood* 2009;113(24):6182–92. [PubMed: 19387008]
35. Arafeh R, Qutob N, Emmanuel R, et al. Recurrent inactivating RASA2 mutations in melanoma. *Nat Genet* 2015;47(12):1408–10. [PubMed: 26502337]
36. Shain AH, Bastian BC. The Genetic Evolution of Melanoma. *N Engl J Med* 2016;374(10):995–6.

37. Kelly JW, Chamberlain AJ, Staples MP, McAvoy B. Nodular melanoma. No longer as simple as ABC. *Aust Fam Physician* 2003;32(9):706–9. [PubMed: 14524207]
38. Huang FW, Hodis E, Xu MJ, Kryukov GV, Chin L, Garraway LA. Highly recurrent TERT promoter mutations in human melanoma. *Science* 2013;339(6122):957–9. [PubMed: 23348506]
39. Horn S, Figl A, Rachakonda PS, et al. TERT promoter mutations in familial and sporadic melanoma. *Science* 2013;339(6122):959–61. [PubMed: 23348503]
40. Schadendorf D, Akkooi ACJ van, Berking C, et al. Melanoma. *The Lancet* 2018;392(10151):971–84.
41. Shitara D, Nascimento MM, Puig S, et al. Nevus-associated melanomas: clinicopathologic features. *Am J Clin Pathol* 2014;142(4):485–91. [PubMed: 25239415]
42. Abu Tahir M, Pramod K, Ansari SH, Ali J. Current remedies for vitiligo. *Autoimmun Rev* 2010;9(7):516–20. [PubMed: 20149899]

## Methods references

43. Zeng H, Jorapur A, Shain AH, et al. Bi-allelic Loss of CDKN2A Initiates Melanoma Invasion via BRN2 Activation. *Cancer Cell* 2018;34(1):56–68.e9. [PubMed: 29990501]
44. Reinius B, Mold JE, Ramsköld D, et al. Analysis of allelic expression patterns in clonal somatic cells by single-cell RNA-seq. *Nat Genet* 2016;48(11):1430–5. [PubMed: 27668657]
45. Pritchard JK, Stephens M, Donnelly P. Inference of population structure using multilocus genotype data. *Genetics* 2000;155(2):945–59. [PubMed: 10835412]
46. Sudmant PH, Rausch T, Gardner EJ, et al. An integrated map of structural variation in 2,504 human genomes. *Nature* 2015;526(7571):75–81. [PubMed: 26432246]
47. Dobin A, Davis CA, Schlesinger F, et al. STAR: ultrafast universal RNA-seq aligner. *Bioinformatics* 2013;29(1):15–21. [PubMed: 23104886]
48. Li B, Dewey CN. RSEM: accurate transcript quantification from RNA-Seq data with or without a reference genome. *BMC Bioinformatics* 2011;12:323. [PubMed: 21816040]
49. Love MI, Huber W, Anders S. Moderated estimation of fold change and dispersion for RNA-seq data with DESeq2. *Genome Biol* 2014;15(12):550. [PubMed: 25516281]
50. Cancer Genome Atlas Network. Genomic Classification of Cutaneous Melanoma. *Cell* 2015;161(7):1681–96. [PubMed: 26091043]
51. Alexandrov LB et al. Signatures of mutational processes in human cancer. *Nature* 500, 415–421 (2013). [PubMed: 23945592]

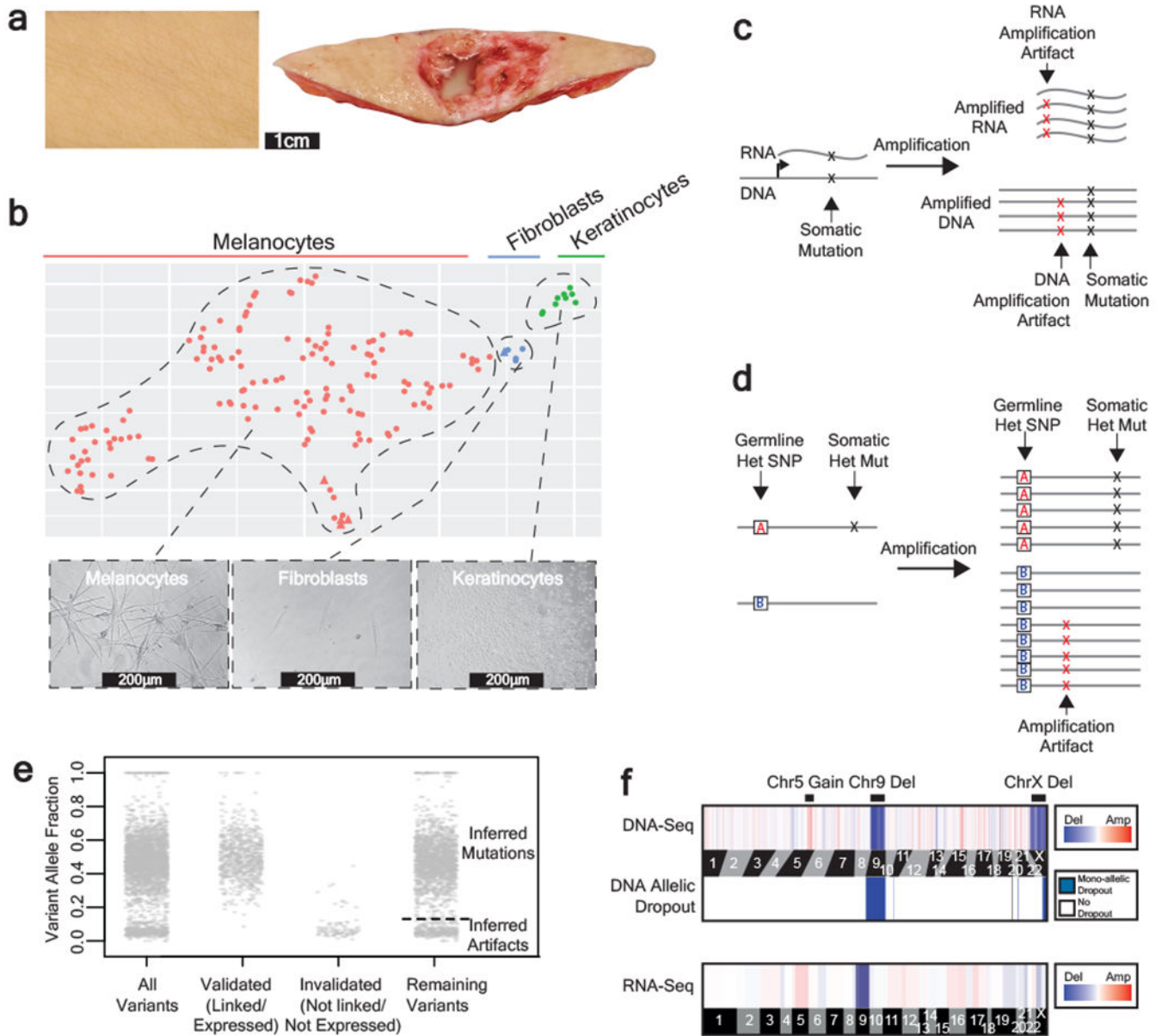


**Figure 1 | A workflow to genotype individual skin cells.**

**a**, Examples of healthy skin from which we genotyped individual cells. Left panel: skin from the back of a cadaver. Right panel: skin surrounding a basal cell carcinoma. **b**, Expression profiles classify the cells that we genotyped into their respective lineages. Each cell is depicted in a t-SNE plot and colored by their morphology. A subset of 5 cells was engineered (see methods) and depicted as triangles. See Extended Data Fig. 1b–c for further details on cell identity. **c-d**, Patterns to distinguish true mutations from amplification artifacts. **c**, Mutations in expressed genes are evident in both DNA- and RNA-sequencing data, whereas amplification artifacts are not. **d**, Germline polymorphisms, distinguished here as “A” and “B” alleles, are in linkage with somatic mutations but not amplification artifacts. **e**, Variant allele fractions from an example cell indicate how we inferred the mutational

status of variants outside of the expressed and phase-able portions of the genome. Variants that were validated as somatic mutations had variant allele fractions (VAFs) around 1 or 0.5, and variants that were invalidated had lower VAFs; however, PCR biases sometimes skewed these allele fractions. Variants that could not be directly validated or invalidated were inferred by their VAF (see methods for details). The dotted line indicates the optimal VAF cut-off to distinguish somatic mutations from amplification artifacts for this particular cell's variants (see Extended Data Fig. 2b for more details). **f**, Copy number was inferred from DNA- and RNA- sequencing depth as well as from allelic imbalance -- an example of a cell with a gain over chr. 5q, loss of chr. 9, and loss of chr. X is shown.

Author Manuscript

Author Manuscript

Author Manuscript

Author Manuscript

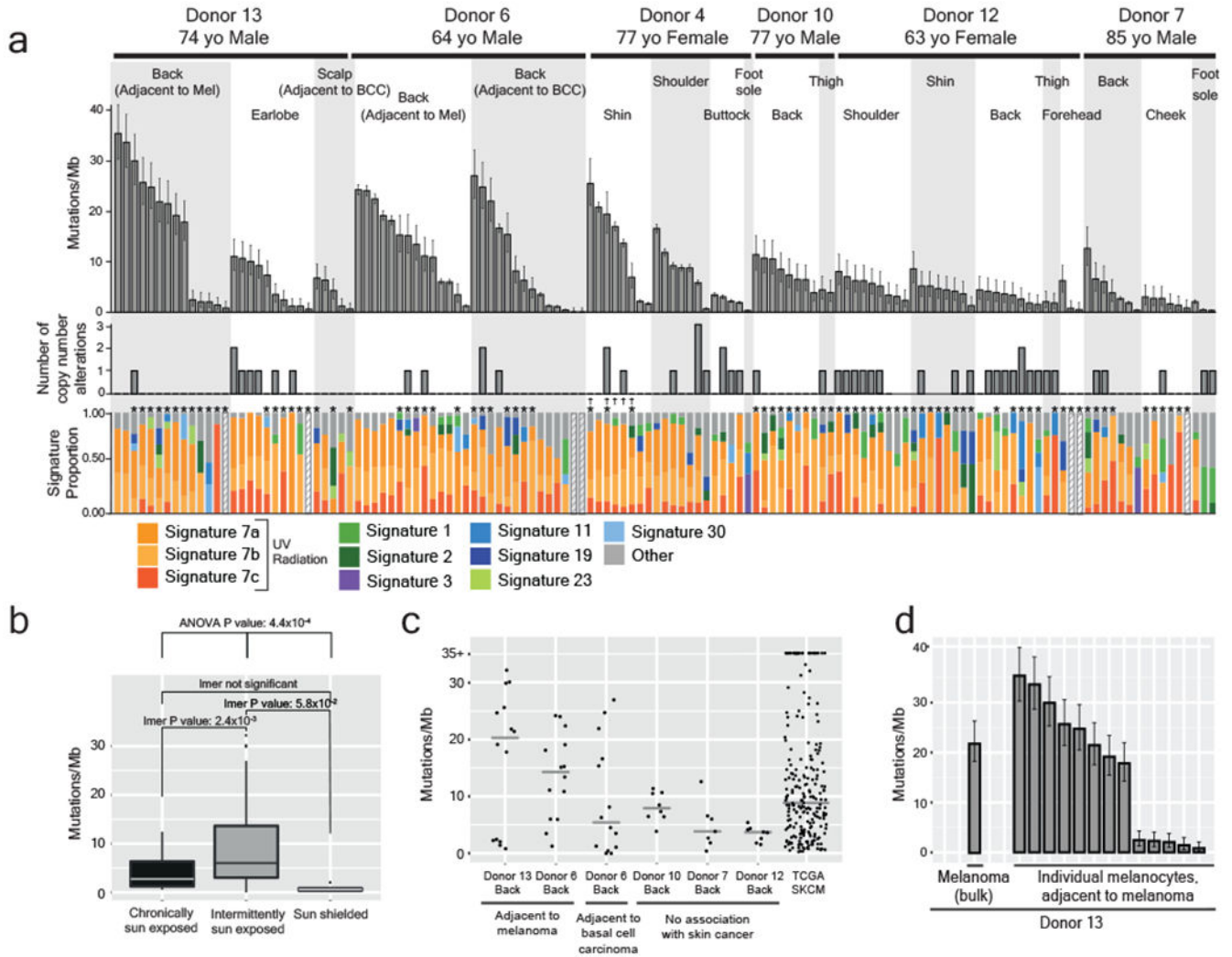


**Figure 2 | The genomic landscape of individual melanocytes from physiologically normal human skin.**

**a**, Top panel: Mutation burden of melanocytes from physiologically normal skin of six donors across different anatomic sites (BCC = Basal Cell Carcinoma, Mel = Melanoma). Middle panel: Number of copy number alterations identified within each melanocyte. Lower panel: The proportion of each cell's mutations that are attributable to established mutational signatures. Each bar represents one cell ( $n=1$ ). Error bars represent 95% confidence intervals determined by two-sided Poisson test. Hashed bars indicate that there were too few mutations for signature analysis. Asterisks denote samples that only underwent targeted DNA-sequencing. Crosses denote *CDKN2A*-engineered cells. **b**, Comparisons between mutation burden of chronically sun-exposed ( $n=24$ ), intermittently sun-exposed ( $n=105$ ), and sun-shielded sites ( $n=4$ ). An ANOVA, comparing the results of linear mixed-effect models both including and excluding sun exposure to account for repeated donor measurements, presented a p-value of  $4.43 \times 10^{-4}$  demonstrating that sun exposure has a significant effect on mutation burden. Pairwise p-values from linear mixed-effects model are also shown (LMER p-values). Each box plot shows the 25<sup>th</sup> and 75<sup>th</sup> percentile of mutation



burdens, where the midline is the data median and outliers are represented as dots. **c**, Mutation burden of site-matched melanocytes adjacent to cancer versus not adjacent to cancer. Melanoma mutation burdens from TCGA are shown as a reference. The median is denoted by a grey line. **d**, Mutation burden of melanocytes as compared to an adjacent melanoma. Each bar represents one cell (n=1). Error bars represent 95% confidence intervals calculated using a two-sided Poisson test.

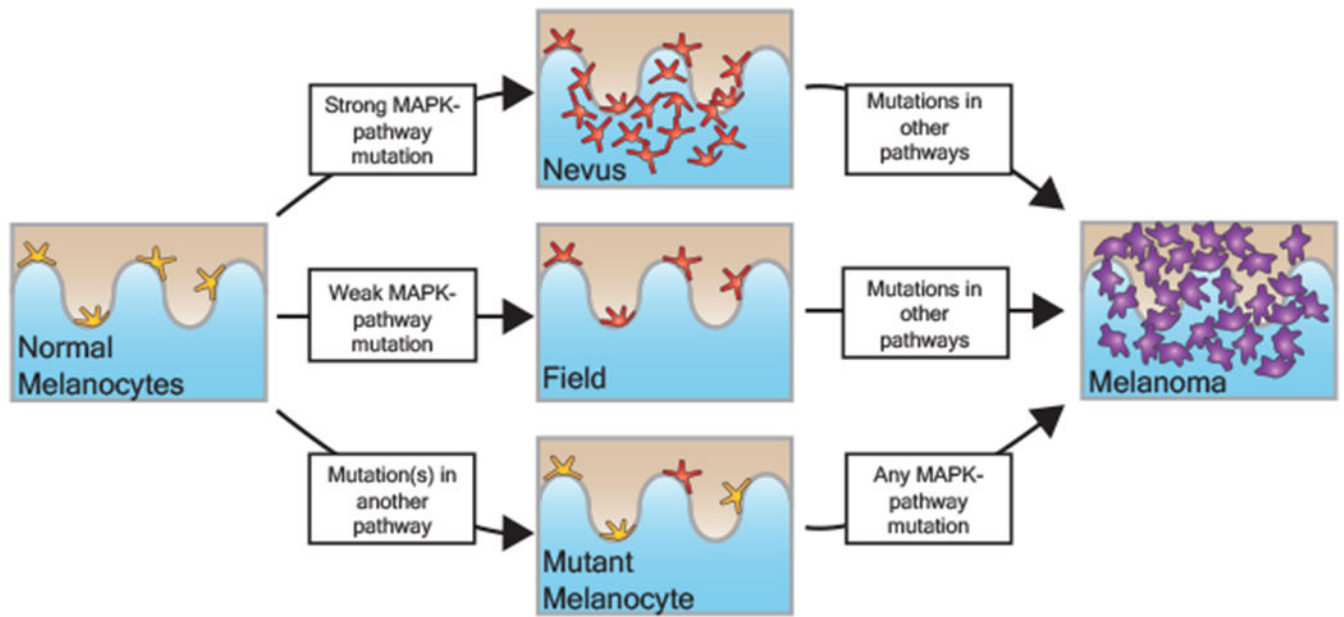


**Figure 3 | Distinct trajectories of melanoma evolution.**

Based on the data shown here and in conjunction with previous genetic, clinical, and histopathologic observations, we propose that melanomas can evolve via distinct trajectories, depending upon the order in which mutations occur. MAPK = Mitogen-Activated Protein-Kinase.

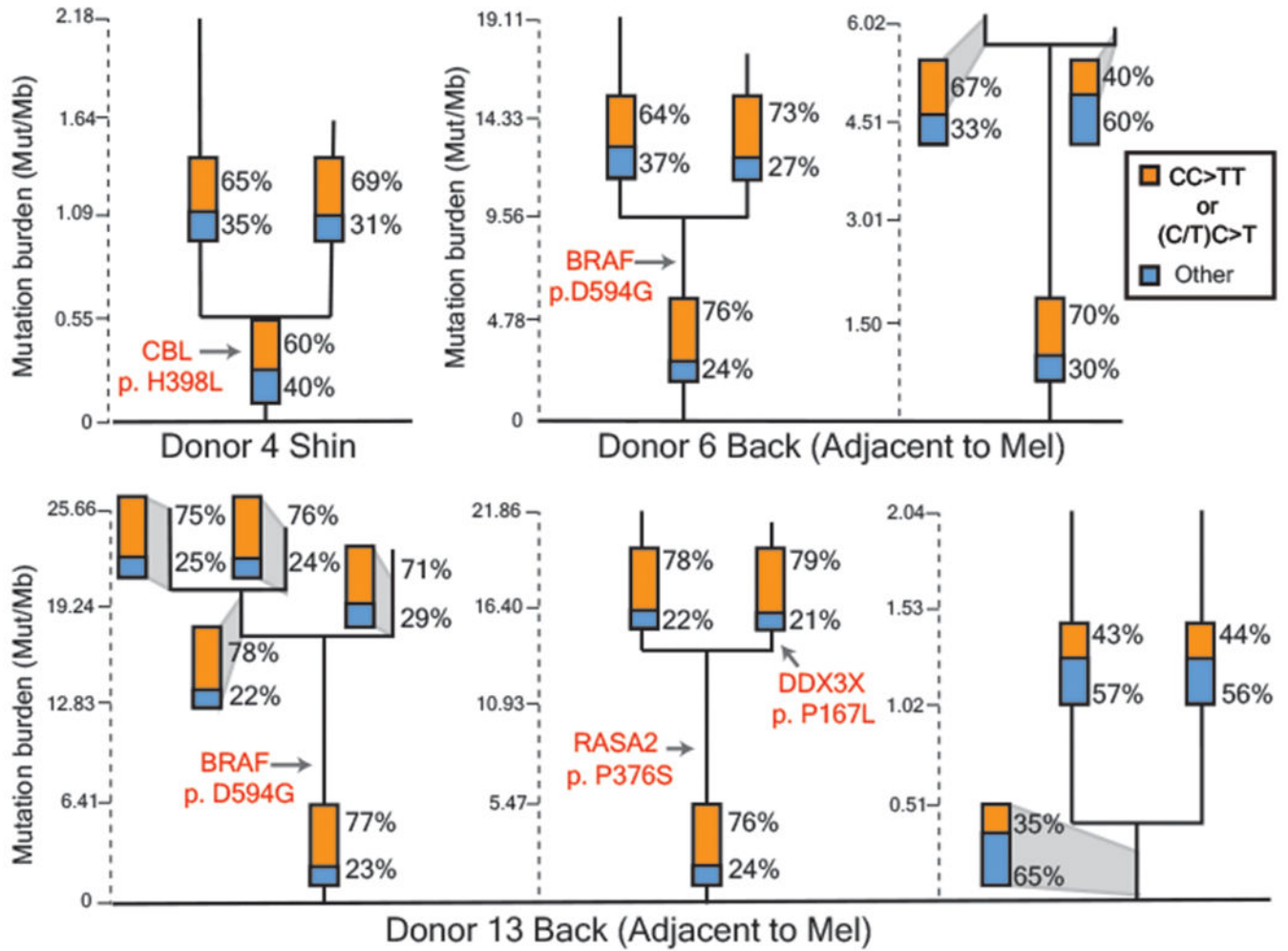


**Figure 4 | Fields of related melanocytes identified in normal human skin.**

Phylogenetic trees in which each branch corresponds to an individual cell. Mutations that are shared between cells comprise the trunk of each tree and private mutations in each cell form the branches. Trunk and branch lengths are scaled equivalently within each tree but not across trees. The proportion of mutations that can be attributed to ultraviolet radiation (CC>TT or (C/T)C>T) is annotated in the bar charts on each tree trunk or branch. Pathogenic mutations and their location on each tree are indicated in red text. Mel = Melanoma.

**Table 1 |  
Pathogenic mutations in melanocytes from normal human skin.**

A curated list of pathogenic mutations in melanocytes found in this study (see methods for details on how they were defined). BCC = Basal Cell Carcinoma, Mel = Melanoma.

Pathway	Hugo Symbol	Protein Change	Donor	Site
MAPK	BRAF	p.G466R	Donor6	Back (adjacent to a BCC)
	BRAF	p.G466R	Donor6	Back (adjacent to a Mel)
	BRAF	p.D594G	Donor6	Back (adjacent to a Mel)
	BRAF	p.D594G	Donor6	Back (adjacent to a Mel)
	BRAF	p.D594G	Donor13	Back (adjacent to a Mel)
	BRAF	p.D594G	Donor13	Back (adjacent to a Mel)
	BRAF	p.D594G	Donor13	Back (adjacent to a Mel)
	CBL	p.H398L	Donor4	Shin
	CBL	p.H398L	Donor4	Shin
	MAP2K1	p.E203K	Donor4	Shoulder
	MAP2K1	p.E203K	Donor10	Thigh
	NF1	p.W1314*	Donor6	Back (adjacent to a BCC)
	NF1	p.P1847L	Donor13	Back (adjacent to a Mel)
	NF1	p.Q2239*	Donor13	Back (adjacent to a Mel)
	NF1	p.R1276*	Donor6	Back (adjacent to a Mel)
	NF1	p.V2511fs	Donor10	Back
	RASA2	p.L83I	Donor6	Back (adjacent to a BCC)
	RASA2	p.P376S	Donor13	Back (adjacent to a Mel)
	RASA2	p.P376S	Donor13	Back (adjacent to a Mel)
	NRAS	p.Q61L	Donor13	Back (adjacent to a Mel)
Cell Cycle	CDKN2A	p.V43M	Donor6	Back (adjacent to a BCC)
	PPP6C	p.R264C	Donor10	Back
Epigenetic	ARID2	p.E1670K	Donor7	Cheek
	ARID2	p.Q1591*	Donor4	Buttock
	ARID2	p.A18V	Donor6	Back (adjacent to a Mel)
	ARID2	p.L202S	Donor6	Back (adjacent to a Mel)
	ARID2	p.P1392L	Donor13	Ear
PI3K	PTEN	p.QYPFEDH87fs	Donor13	Ear
RNA Processing	DDX3X	p.P167L	Donor13	Back (adjacent to a Mel)